Chemical Geology 542 (2020) 119595

Contents lists available at ScienceDirect

Chemical Geology

journal homepage: www.elsevier.com/locate/chemgeo

δD and $\delta^{18}O$ variations of the magmatic system beneath Deception Island volcano (Antarctica): Implications for magma ascent and eruption forecasting

A.M. Álvarez-Valero[a,b,*], G. Gisbert[c], M. Aulinas[d], A. Geyer[e], G. Kereszturi[f], A. Polo-Sánchez[a], E. Núñez-Guerrero[a,b], H. Sumino[g], J. Borrajo[h]

[a] Department of Geology, University of Salamanca, Spain
[b] Laboratory of Stable Isotopes (NUCLEUS), University of Salamanca, Spain
[c] Institute of Geosciences, CSIC, Madrid, Spain
[d] Department of Mineralogy, Petrology and Applied Geology, University of Barcelona, Spain
[e] Institute of Earth Sciences Jaume Almera, ICTJA, CSIC, Barcelona, Spain
[f] Volcanic Risk Solutions, School of Agriculture and Environment, Massey University, Palmerston North, New Zealand
[g] Department of Basic Sciences, University of Tokyo, Japan
[h] Department of Physics, Engineering and Medical Radiology, University of Salamanca, Spain

ARTICLE INFO

Editor: Donald Dingwell

Keywords:
Stable isotopes
Active volcano
Magma degassing
Deception Island
Antarctica
Volcanic hazard
Pre-eruptive magmatic conditions

ABSTRACT

Geochemistry of volatiles in active volcanoes provides insights into the magmatic processes and evolution at depth, such as magma evolution and degassing, which can be implemented into volcanic hazards assessment. Deception Island is one of the most active volcanoes in Antarctica, with more than twenty explosive eruptions documented over the past two centuries. Hydrogen and oxygen isotopic variations in the volatiles trapped in the Deception Island rocks (glass and melt inclusions in phenocrysts) provide essential information on the mechanisms controlling the eruptive history in this volcanic suite. Thus, understanding the petrological and related isotopic variations in the island, has the potential to foresee the possible occurrence and its main eruptive features of a future eruption.

The new isotopic results of this study combined with exhaustive petrologic knowledge reveal in Deception Island (i) fast ascent and quenching of most magmas, preserving pre-eruptive magmatic signal of water contents and isotopic ratios, with local modification by rehydration due to glass exposition to seawater, and by meteoric and fumarolic waters; (ii) a plumbing system(s) variable with time and currently dominated by closed-system degassing leading to explosive eruptions; (iii) control on the interactions of ascending magmas with the surface waters producing hydrovolcanic activity throughout the two main fault systems in Deception Island and at different magma stagnation depths. These results can be considered in further studies of volcanic monitoring to improve the capability to interpret geophysical data and signals recorded during volcanic unrest episodes, and hence, forecast volcanic eruptions and related hazards.

1. Introduction

Water is the most abundant volatile in magmatic and volcanic systems. Therefore, its oxygen and hydrogen isotopic ratios have the potential to provide information on the magma source and evolution, on pre- and *syn*-eruptive volcanic processes, and on the possible rehydration modification of the volcanic products. Oxygen is the most abundant element in the Earth's mantle, crust and fluids, and therefore its isotopic knowledge is essential in tracking many environmental processes at depth and surface, including magma genesis, degassing and eruptive processes (e.g. Bindeman, 2008). On the other hand, hydrogen isotopic ratio (D/H) in magmatic and volcanic systems is essential for understanding the origin and cycle of our planet's water, as well as the evolution of a particular volcano from magma source at depth to its eruption (e.g. Jambon and Zimmermann, 1990; Shaw et al., 2008). Hydrogen in magmas is little affected by host rock assimilation, therefore D/H in freshly erupted volcanic rocks mostly depends on the original δD of the parental magma, volcanic degassing history, and pre-

* Corresponding author at: Department of Geology, University of Salamanca, Spain.
E-mail address: aav@usal.es (A.M. Álvarez-Valero).

https://doi.org/10.1016/j.chemgeo.2020.119595
Received 19 July 2019; Received in revised form 13 March 2020; Accepted 21 March 2020
Available online 23 March 2020

eruptive incorporation of external water (e.g. DeGroat-Nelson et al., 2001; Hoefs, 2009; Tuffen et al., 2010). In addition, volcanic rocks, especially their volcanic glass components, are susceptible to secondary rehydration by meteoric waters, which are characterized by different δD and δO values (e.g. Hoefs, 2009) controlled by factors such as latitude, temperature, and distance to the ocean. Thus, constraining the original magmatic δD and $\delta^{18}O$ signals and subsequent potential rehydration to their present composition requires the comparison with reference data from the volcanic rocks and the sources of external water (e.g. meteoric waters). This in turn is fundamental for the knowledge on the magma dynamics and degassing mechanisms to better assess the most likely eruptive scenarios for future eruptions (e.g. Vergiolle and Jaupart, 1986; Cashman and Mangan, 1994; Lange, 1994; Seligman et al., 2016).

Deception Island in the South Shetland Islands (Antarctica) is an active volcanic island hosting a caldera that formed between c. 8300 and 3980 years BC (Oliva-Urcia et al., 2015; Antoniades et al., 2018). During this caldera-forming event, over 60 km^3 of magma erupted (Martí et al., 2013), forming a 6 × 10 km caldera (Geyer and Martí, 2008). Tens of post-caldera monogenetic vents have erupted in historical times and as recent as 1970, with at least 20 recorded eruptions in the last two centuries (Orheim, 1972; Roobol, 1980; Smellie, 2002a; Bartolini et al., 2014). Historical eruptions destroyed or severely damaged many scientific and whaling stations on the island (Baker et al., 1975; Roobol, 1982; Smellie, 2001), mainly due to phreatomagmatic eruptions resulting from magma-water interactions and associated jökulhlaup. In addition, the presence of post-caldera tephras from Deception Island in distal (> 500 km in distance) marine sediments (Delmas et al., 1992), and ice cores (Moreton and Smellie, 1998; Fretzdorff and Smellie, 2002) reveals that Deception Island volcano can produce much larger scale eruptive activity than indicated by the historical records (Antoniades et al., 2018). Nowadays, Deception Island holds two scientific bases and receives > 15,000 tourists annually (IAATO, International Association of Antarctica Tour Operators, 2018), being one of the top attractions of the Antarctic Peninsula. Therefore, future volcanic activity is a serious concern for scientists, military staff and tourists staying in the island or nearby.

In this paper, we utilize hydrogen and oxygen isotopic ratios of volcanic glasses and phenocrysts to investigate the processes that controlled the magmatic evolution and eruption dynamics of Deception Island. Hydrogen and oxygen isotopes are key components to unravel shallow degassing and interaction mechanism between external water and ascending magma. Moreover, such isotopic data can also constrain potential coupling between tectonic lineament and fluid pathways to the surface, aiding volcanic hazard assessment. Understanding these factors and their influence on the styles of volcanic activity at Deception Island will contribute to enhance the interpretation of geophysical data recorded during volcanic unrest episodes and the volcanic eruptions forecasting prior small-volume, monogenetic-style eruptions.

2. Geological setting

Deception Island is located next to the intersection between the extension of the Hero Fracture Zone and the southwestern end of the Bransfield Strait. The Bransfield Strait is a NE–SW, 500-km-long and 100-km-wide, extensional basin that separates the South Shetland continental microplate from the Bransfield Platform (Grad et al., 1992; Catalán et al., 2013, 2014) (Fig. 1a). Deception Island is a volcanic system that was built on the northern shoulder of the Bransfield rift, which is a 15–20 km wide extensional structure located at the center of the Bransfield Strait and was produced by back-arc extension during the Late Cenozoic linked to subduction of the Phoenix Plate beneath the Antarctic Plate (González-Ferrán, 1985; Birkenmajer et al., 1990; Birkenmajer, 1992). The complex regional geodynamics of subduction and back-arc spreading processes directly influenced the timing and composition of magmatism in the region (Košler et al., 2009; Haase et al., 2012; Kraus et al., 2013; Geyer et al., 2019), which is mostly concentrated in Deception, Penguin and Bridgeman Islands during the Quaternary (Birkenmajer et al., 1990; Hole et al., 1994; Haase et al., 2012).

Deception Island is an emerged composite volcano, forming a horseshoe-shaped island with a diameter of 15 km. The island itself features volcanic collapse caldera that is filled by sea water, Port Foster, with a maximum present-day water depth of 190 m (Figs. 1, 2). This volcano has a 30 km basal diameter and rises 1400 m from the seafloor to a maximum height of c. 540 m above sea level (Luzón et al., 2011). All rocks exposed in Deception Island are thought to be younger than 100 kyr based on tephra chronostratigraphic data collected in the Shetlands area (e.g. Smellie, 2001).

The island's volcanic evolution is marked by a caldera collapse at c. 8300–3980 years BC (Oliva-Urcia et al., 2015; Antoniades et al., 2018), which subdivides the history of this island into three main phases: pre-, *syn*- and post-caldera (Fig. 2). The pre-caldera episode (< 750 kyr; Valencio et al., 1979) is characterized by the growth of numerous seamounts that coalesced to form a subaerial volcanic shield (Smellie, 2002a). The caldera formation event, hereafter referred to as *syn*-caldera, deposited ignimbrites which are several tens of meters thick (Outer Coast Tuff Formation), and it is a distinctive stratigraphic marker of the whole island. The post-caldera stage is characterized by the formation of > 70 scattered small-volume, monogenetic eruptive centers. This phase includes volcanic material erupted in recent years, between 1829 and 1970 CE (Smellie, 2002a; Martí et al., 2013). The post-caldera phase is dominated by explosive eruptions (< 0.1 km^3 and VEI 2–3; Smellie, 2001; Pedrazzi et al., 2014, 2018), forming mostly fissure-sourced scoria, and tuff cone and tuff ring volcanoes. The last eruptions occurred in 1967, 1969, and 1970 (e.g. Baker et al., 1975; Smellie, 2001, 2002a).

The volcanic rocks at Deception Island are tholeiitic, ranging in composition from basalts to trachydacites and rhyolites, and following an alkalinity-increasing trend at the upper end of the subalkaline field in the Total Alkali vs. Silica diagram (TAS, Fig. 4) (e.g. Aparicio et al., 1997; Smellie, 2002a; Geyer et al., 2019). Trace element compositions show no significant differences between pre-, syn-, and post-caldera rocks (Geyer et al., 2019). This indicates a magma source similar to that of subalkaline Bransfield Rift rocks with the minor influence of subduction component, pointing out its different source from other South Shetland Islands magmas (see also Aparicio et al., 1997; Smellie, 2002a). Deception Island magmas also indicate a high partial melting degree (Geyer et al., 2019), which is suggested to be the cause for the distinctive higher alkalinity of its rocks. Chemical composition of the glass population in the samples are alike to the whole rock, mainly ranging from basaltic to trachyandesitic compositions, with minor trachytic and rhyolitic ones, and also show similar chemical trends (see Geyer et al., 2019, for more details of the petrologic and geochemical features of Deception Island samples).

Two main sets of tectonic lineaments crustal faults, which relate to the volcanic activity in the island, have been described by De Rosa et al. (1995): NE-SW and NW-SE faulting systems. The island's seismicity is more active along the NE–SW direction fractures set (e.g. Fumarole Bay to Pendulum Cove in the area of the destroyed Chilean scientific base), matching with the areas of highest geothermal activity (Ibáñez et al., 2000). The most recent and shallow earthquakes in the island were caused by hydrofracturing of the crust because of the volume increment related to vaporization mechanisms (e.g. Correig et al., 1997; Kusakabe et al., 2003, 2009). These fault systems are considered to be preferential paths for the escaping of magmatic volatiles towards the surface (e.g. Holland et al., 2011; Schipper et al., 2013).

The main volcanic hazards in the island are related to ash and lapilli fallout, ballistic blocks and bombs, and subordinate dilute pyroclastic density currents and destabilization driven mass wasting (e.g. Smellie, 2002b; Bartolini et al., 2014; Pedrazzi et al., 2018). There are several potential sources of external water (e.g. sea and small lakes or ponds,

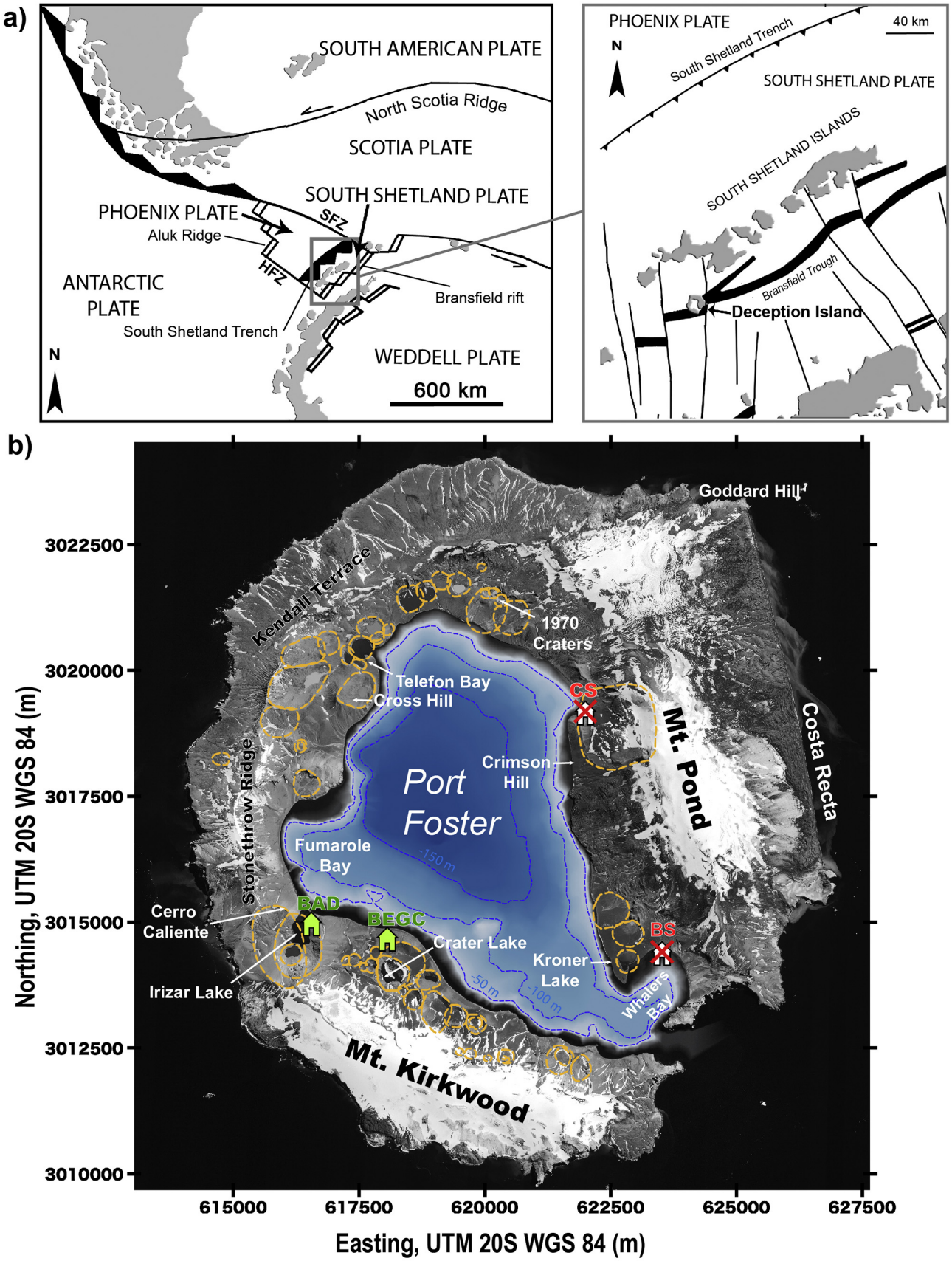

Fig. 1. (a) Simplified regional tectonic map and location of the South Shetland Islands (modified from Martí et al., 2013). HFZ (Hero Fracture Zone), SFZ (Shetland Fracture Zone). (b) Deception Island orthophotomap (data obtained from Spatial Data Infrastructure for Deception Island SIMAC, Torrecillas et al. (2006)) with bathymetric data (Barclay et al., 2009; Ibáñez et al., 2017). Existing and destroyed scientific stations are: BAD: Base Antártica Decepción (Argentinean Scientific base); BEGC: Base Española Gabriel de Castilla (Spanish scientific base); BS: Remains of the British scientific base; CS: Remains of the Chilean scientific base.

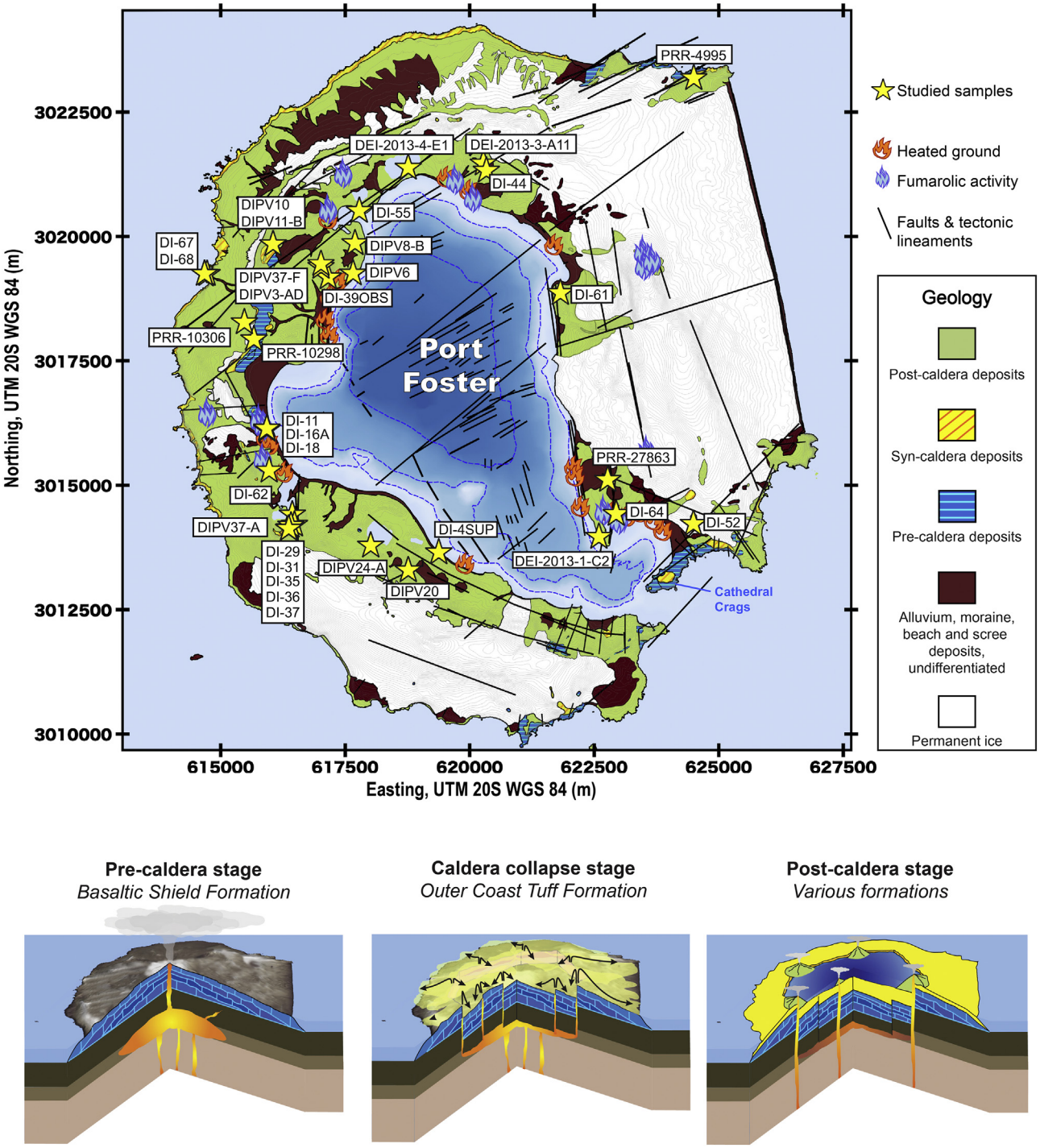

Fig. 2. Simplified geological map of Deception Island (modified from Martí et al., 2013), showing the location of the analyzed samples, and distribution of the two main tectonic fault sets described by De Rosa et al., 1995 (i.e. NW-SE and NE-SW). The three cartoons at the bottom present the volcanic evolution of the island from the main cone formation, followed by the caldera collapse and finishing in the post-caldera eruptive episodes.

aquifers and glacier melt-water) that can quickly shift volcanic eruptions to become highly explosive due to water-magma interaction (Pedrazzi et al., 2014, 2018). The fact that Deception Island has produced more than twenty eruptions over the past two centuries (e.g. Orheim, 1972; Roobol, 1982; Smellie, 2002a), and many unrest episodes in 1992, 1999 (Ibáñez et al., 2003; Rosado et al., 2019) and 2014–2015 (Almendros et al., 2015; Rosado et al., 2019), imply a high probability for new eruptions in the near future.

3. Samples and analytical methods

At Deception Island, the increased volcanic activity after the caldera formation has buried most of pre- and *syn*-caldera deposits. However, a wide suite of representative samples has been collected during multiple field campaigns between 2011 and 2018. We sampled at 12 locations distributed over the entire island (Fig. 2), covering pre-, syn- and post-caldera materials, for the H and O isotopic analysis in glasses (32 samples, Table 1) and melt inclusions-bearing plagioclase and olivine phenocrysts (7 samples, Table 1). In addition, we complemented our

Table 1
δD and $\delta^{18}O$ isotope results of DI juvenile fragments correlated to fault sets and depth provenances. *: data from De Rosa et al. (1995); **: data from Geyer et al. (2019); ***: post-caldera sample on the geological map of Martí et al. (2013) (next to pre-caldera and/or syn-caldera contacts). For sample DI-67 (Ol-Px phenocryst) olivine and pyroxene crystals within the same assemblage were used for δD and $\delta^{18}O$ analysis, respectively. PDC: pyroclastic density current. International Geo Sample Number (IGSN) codes refer to an open online database of archived metadata (www.geosamples.org). PRR samples were loaned by the The Polar Rock Repository (PRR) and Byrd Polar and Climate Research Center (BPCRC), n.d (http://research.bpcrc.osu.edu/rr/) on summer 2018. Samples PRR-10298, PRR-10306, PRR-27863 were collected by C.H. Shultz in 1970, and sample PRR-4995 by Pamela J. Ellerman Lundstrom in 1984.

Sample	IGSN	Type of sample	Milligrams	Episode	Location area	$\delta^{18}O$ (± 0.15) ‰	δD (± 1) ‰	H2O %	Fault direction*	Depth (km)**
DEI-2013-1-C2	IED1301C2	Pyroclastic material	391.1	Post-caldera	Kroner Lake	5.6	−84.3	0.6	NE-SW	8.1
DEI-2013-3-A11	IED1303A11	Pyroclastic material	341.2	Post-caldera	1970	5.5	−70.3	0.5	NE-SW	7.7
DEI-2013-4-E1	IED1304E1	Pyroclastic material	367.3	Post-caldera	1970	5.6	−88.1	0.5	NE-SW	7.7
DI-37	IED110037	PDC	680.1	Post-caldera	Irizar Lake	5.4	−61.0	1.1	?	
DI-37	IED110037	Pl-phenocryst	511.1	Post-caldera	Irizar Lake	6.0	−93.7	0.5		33.5
DI-39OBS	IED11039OBS	Obsidian	300.2	Post-caldera	Cross Hill	5.8	−137.7	0.1	?	1.9
DI-44	IED110044	Lapilli	480.7	Post-caldera	1970	5.9	−58.1	0.5	NE-SW	8.1
DI-4SUP	IED11004SUP	Lapilli	339.0	Post-caldera	Crater Lake	5.6	−109.8	0.2	NW-SE	11.2
DI-55	IED110055	Lapilli	202.4	Post-caldera	1967	5.9	−65.0	0.3	NE-SW	6.2
DI-61	IED110061	Lapilli	705.8	Post-caldera	Crimson Hill	6.0	−31.1	0.2	NE-SW?	15.8
DI-62	IED110062	PDC	481.8	Post-caldera	Cerro Caliente	6.2	−77.8	1.1	NW-SE	
DI-64	IED110064	Lapilli	462.3	Post-caldera	Kroner Lake	6.0	−37.5	0.5	NE-SW	8.1
DIPV20	IED180020	Vesiculated lava	713.7	Post-caldera	Crater Lake	4.8	−85.4	0.5	NE-SW	
DIPV20	IED180020	Pl-phenocryst	399.0	Post-caldera	Crater Lake	5.0	−110.4	0.2		
DIPV24-A	IED18024A	Juvenile fragment	383.2	Post-caldera	Crater Lake	5.5	−55.3	0.5	?	
DIPV3-AD	IED18003AD	Juvenile fragment	533.8	Post-caldera	Cross Hill	5.8	−54.2	0.5	NE-SW	
DIPV37-F	IED18037F	Banded pumice	360.1	Post-caldera	Cross Hill	5.8	−57.9	2.0	NE-SW	
DIPV6	IED180006	Juvenile fragment	426.1	Post-caldera	Cross Hill	5.6	−75.5	0.2	NE-SW	
DIPV8-A	IED18008A	Pumice	648.5	Post-caldera	Cross Hill	5.4	−55.4	0.3	NE-SW	
PRR-27863	PRR027863	Lava	744.7	Post-caldera	Kroner Lake	6.1	−85.7	0.03	?	
PRR-10306	PRR010306	Lava	490.2	Post-caldera	Stonethrow Ridge	5.6	−107.5	0.04	?	
DI-16A	IED11016A	Scoria	299.1	Pre-caldera	Fumarole Bay	5.6	−94.7	0.7	NW-SE	27.7
DI-18	IED110018	PDC	338.1	Pre-caldera	Fumarole Bay	4.6	−111.3	2.2	NW-SE	31.5
DI-18	IED110018	Pl-phenocryst	670.7	Pre-caldera	Fumarole Bay	6.0	−112.9	0.4		31.5
DIPV10	IED180010	Lava	636.7	Pre-caldera(***)	Cross-Hill	5.3	−105.0	0.1	?	
DIPV11-B	IED18011B	Scoria	373.1	Pre-caldera(***)	Cross-Hill	4.5	−91.4	0.1	?	
DIPV37-A	IED18037A	Lithic	770.1	Pre-caldera	Irizar Lake	6.1	−102.1	0.2	?	
PRR-10298	PRR010298	Pyroclastic breccia	647.1	Pre-caldera	Fumarole Bay	5.8	−92.8	0.7	?	
DI-67	IED110067	Pl-phenocryst	733.3	Crystal mush/ plutonic	Kendall Terrace	6.0	−107.6	0.1		39.2
DI-67	IED110067	Ol-Px-phenocryst	661.3	Crystal mush/ plutonic	Kendall Terrace	5.6	−116.2	0.1		39.2
DI-11	IED110011	Pipe breccia	558.8	Pipe breccia	Fumarole Bay	6.1	−110.1	1.0	NW-SE	19.2
DI-29	IED110029	PDC	245.8	Syn-caldera	Irizar Lake	4.9	−85.3	0.5	NW-SE	16.9
DI-31	IED110031	Scoria	328.4	Syn-caldera	Irizar Lake	5.8	−125.2	0.7	NW-SE	11.9
DI-35	IED110035	Scoria	361.2	Syn-caldera	Irizar Lake	5.5	−84.2	0.2	NW-SE	15.4
DI-35	IED110035	Pl-phenocryst	835.9	Syn-caldera	Irizar Lake	6.0	−145.7	0.1		15.4
DI-36	IED110036	Scoria	412.0	Syn-caldera	Irizar Lake	5.5	−89.4	0.3	NW-SE	14.2
DI-52	IED110052	Scoria	543.4	Syn-caldera(***)	Whalers Bay	5.6	−84.0	0.3	?	25.0
DI-68	IED110068	PDC	557.5	Syn-caldera	Kendall Terrace	5.3	−91.2	1.2	NE-SW	
DI-68	IED110068	Pl-phenocryst	530.5	Syn-caldera	Kendall Terrace	5.8	−114.2	0.2		
PRR-4995	PRR004995	Hyaloclastite	620.0	Syn-caldera(***)	Goddard Hill (N Coast)	5.6	−83.4	1.2	NE-SW	

sampling with four additional rock samples from the Polar Rock Repository (PRR samples in Table 1) (http://research.bpcrc.osu.edu/rr/). In order to make the results and sample archives of this work accessible to the broader community, all samples have been registered in the online System for Earth Sample Registration database (www.geosamples.org). Registered users can search the database to retrieve sample metadata and information about archived material.

3.1. Summary of petrologic features

The **pre-caldera** deposits mainly consist of lava samples (mostly basaltic to basaltic-andesitic and basaltic-trachyandesitic) and hyaloclastite breccia clasts. These clasts show porphyritic texture of subhedral phenocrysts, mostly plagioclase and olivine hosting melt inclusions (Fig. 3a, b) within a fine-grained or glassy groundmass dominated by plagioclase microlites, and palagonitized scoria fragments. They also show thin, microlitic, glassy margins with local palagonization, whereas the cores of larger fragments are widely unaltered. The less altered microdomains show larger-size vesicles than the more altered ones. Zeolite group mineral phases are locally present filling vesicles (Fig. 3c).

The ***syn*-caldera** samples represent a fine-grained welded ignimbrite, which consists of juvenile scoria and lithics of mafic lava fragments from the pre-caldera phase, both embedded within a glassy, yellowish matrix (Fig. 3c). Locally, platy shards and phenocrysts of pyroxene, olivine and plagioclase are present within the matrix. Glass components are altered to palagonite, similar to the pre-caldera samples.

The **post-caldera** deposits consist of dark scoria fragments with a vitric aspect, and locally include lithic fragments. Juvenile pyroclasts present an aphanitic groundmass that contains scarce crystals up to 10 vol% of the total rock volume. These are mainly microlites, needle-

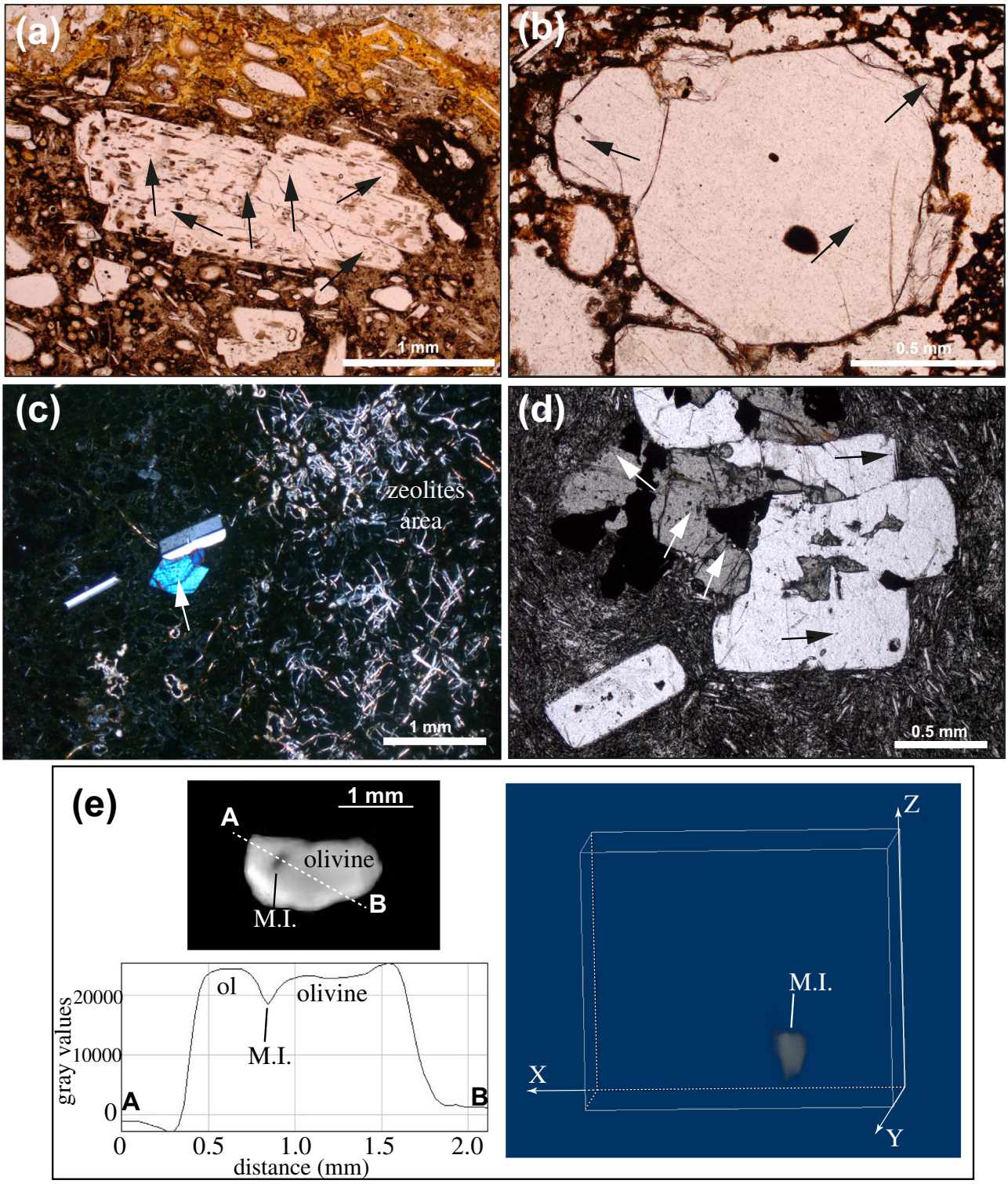

Fig. 3. Microscopic views of melt inclusions (solid white and black arrows)-bearing phenocrysts within: (a) plagioclase in a sideromelane + palagonitic glassy matrix of a pre-caldera sample (plane-polarized light); (c) pre-caldera olivine (cross-polaralized light). This image also highlights the late hydration in the sample matrix through the occurrence of zeolites; (b) *syn*-caldera olivine (plane polarized light); and (d) plagioclase and olivine immersed in a microlitic matrix in a post-caldera sample (plane polarized light); (e) Images of a micro-computed tomography (micro-CT) analysis to observe (and not destroy) the melt inclusions within an olivine crystal (DI-67) before melting it to extract their volatiles and determine the stable isotope ratios. The gray scale diagram allows estimating the melt inclusion's size (c. 0.15 mm in diameter). The three-dimensional (3D) reconstruction (enlarged scale 1:3) shows the precise shape of the melt inclusion within the olivine crystal cut as a parallelepiped (axes in mm: X: 0.7; Y: 0.45; Z: 0.6). An Argus (SUINSA Medical Systems) microtomograph was used with scans performed at 40 kV and 400 μA (effective transverse and axial fields of view of 6.7 and 4.8 cm, respectively). Samples were set on a rotation stage, and transmission images were obtained for each 0.5° of rotation with a total of 720 images. The isotropic pixel edge size is 30 μm. 3D analysis was reconstructed from the transmission images using ImageJ software (Abràmoff et al., 2004).

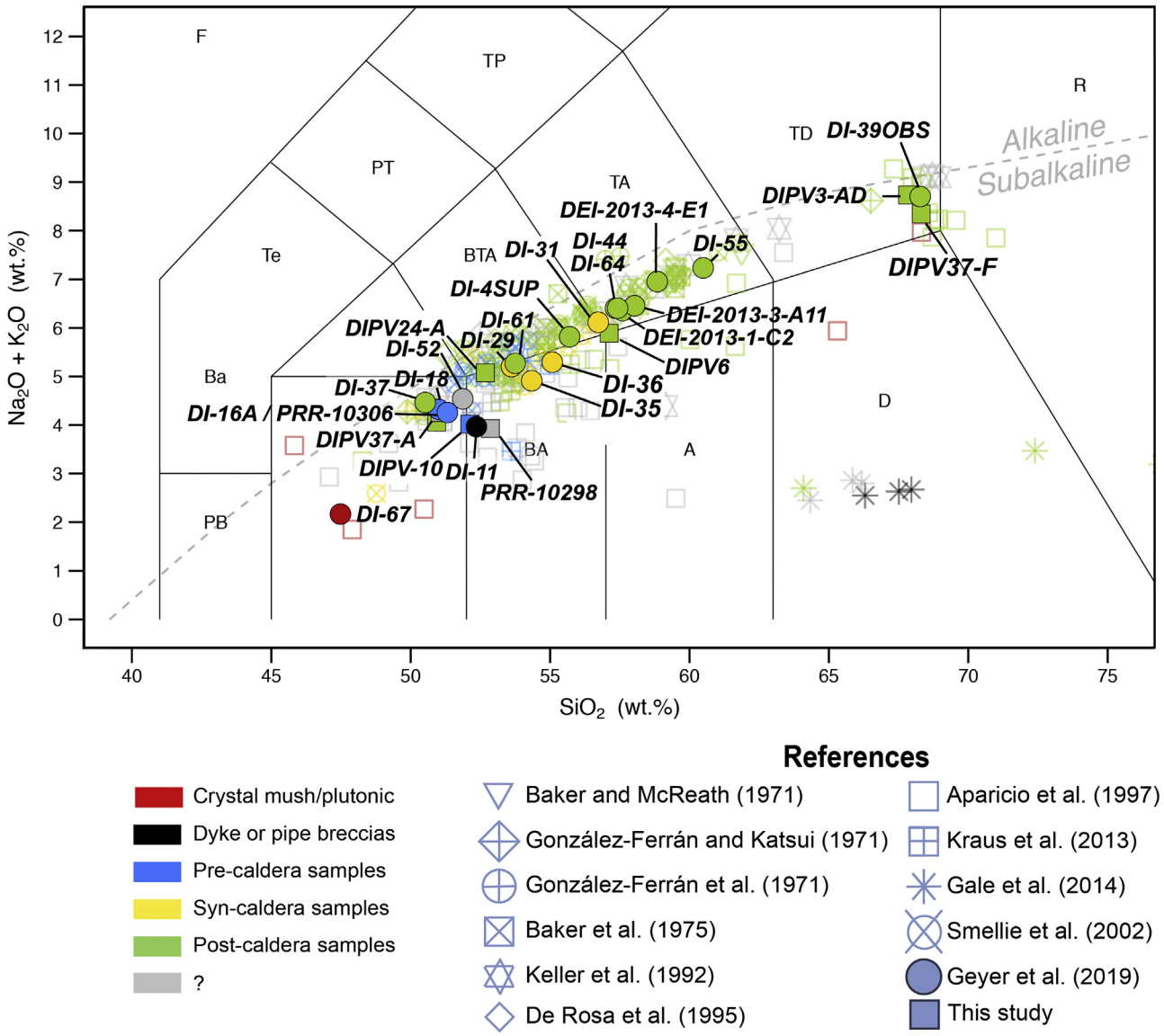

Fig. 4. Total Alkali vs. Silica diagram (Le Bas et al., 1986) for the DI samples. Major elements normalized to 100% (anhydrous) with Fe distributed between FeO and Fe_2O_3 according to Middlemost (1989).

shaped laths of plagioclase and microcrystals (≪1 mm) of euhedral clino- and ortho-pyroxene and rare olivine. Locally, minor larger subeuhedral plagioclase phenocrysts rich in melt inclusions are present in basalts and basaltic andesites (Fig. 3d). At Cross Hill volcano pumice and obsidian pyroclasts were collected; these show the typical vesicular microtexture and oriented plagioclase and opaque microlites, respectively (see Geyer et al., 2019, for more petrological details). In addition to pyroclastic deposits, four lava flow samples were studied. These present a holocrystalline microtexture mostly consisting of plagioclase, olivine and opaque phenocrysts within a microcrystalline matrix of dominant locally oriented plagioclase and minor corroded olivine (Fig. 3d). Alteration is observed in local pre-, syn- and post-caldera juvenile pyroclasts, which transforms sideromelane (quenched glass) to yellowish palagonite.

3.2. Isotopic analysis

For the isotopic analysis of glass we selected the less altered samples to avoid late isotopic modification by weathering. For each sample, we exposed its apparent fresh core by cutting several centimeters of material from the surface. Then, we prepared and petrographically studied rock fragments to confirm total absence of secondary minerals, e.g. zeolites in pre-caldera samples (Fig. 3c), and selected the largest melt-inclusion-bearing phenocrysts (Fig. 3e). Finally, we crushed and sieved (> 400 μm grain size) selected fragments, and manually separated the freshest glass grains and phenocrysts.

The hydrogen and oxygen isotopic analyses were carried out at the Servicio General de Análisis de Isótopos Estables (NUCLEUS - University of Salamanca, Spain). Oxygen in glass and phenocrysts was extracted by fluorination (Clayton and Mayeda, 1963) employing a Synrad 25W CO_2 laser (Sharp, 1990) and ClF_3 as reagent (e.g. Borthwick and Harmon, 1982), and oxygen isotope ratios were measured on a VG-Isotech SIRA-II dual-inlet mass spectrometer. Both internal and international reference standards (NBS-28, NBS-30) were run to check accuracy and precision. Results are reported in $\delta^{18}O$ notation relative to the Vienna Standard Mean Ocean Water (V-SMOW) standard, using a $\delta^{18}O$ value of 9.6‰ for NBS-28 (quartz) for the mass spectrometer calibration. Long-term reproducibility for repeated determination of reference samples was better than ± 0.2‰ (1σ).

D/H ratios were determined on another SIRA-II mass spectrometer on H_2 gas obtained by reduction over hot depleted-U of the water released by induction heating of samples. A vacuum line (Bigeleisen et al.,

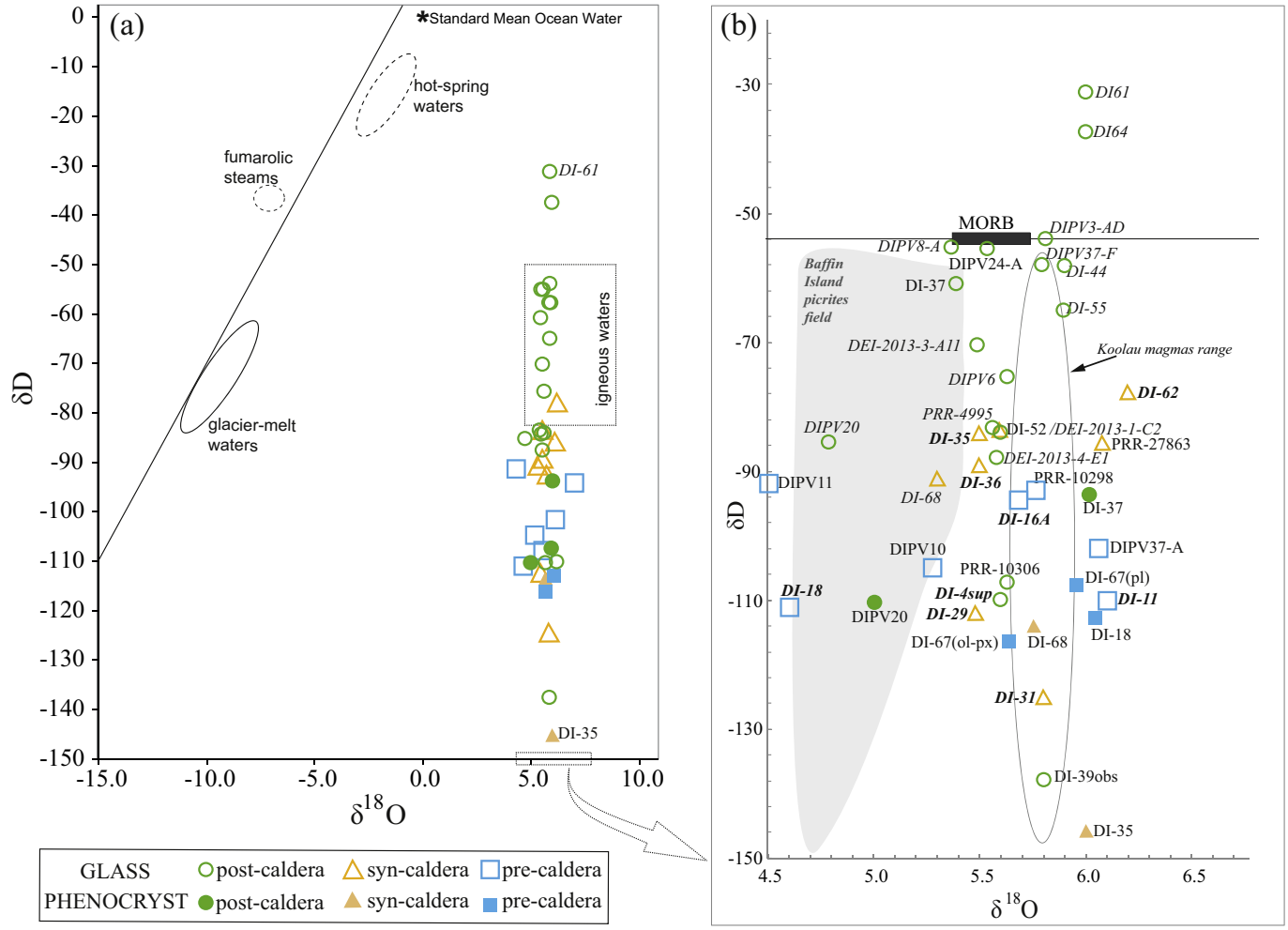

Fig. 5. (a) Plot of δD vs $\delta^{18}O$ as a function of their stratigraphic position (pre-, syn- and post-caldera). Hot-spring, fumarolic and glacier-melt waters data (ellipses) correspond to the local values from Kusakabe et al. (2009); (b) Detail of the same diagram in which samples are grouped according to their connection to the two main tectonic fault systems in the island, i.e. NE-SW (sample name in *italics*) vs. NW-SE (sample name in ***bold-italics***). Koolau and Baffin data is from Hallis et al. (2015).

1952), following the procedures described by Godfrey (1962) with modifications (Jenkin, 1988), was used for gas extraction. Samples (i.e. glass and phenocrysts) were loaded into degassed platinum crucibles that were placed in quartz reaction tubes and heated under vacuum to 125 °C overnight to remove any adsorbed H_2O. Results are reported in δD notation relative to the V-SMOW standard, using a δD = −66.7‰ for NBS-30 (biotite) for the mass spectrometer calibration. The amount of the H_2 recovery is known by a baratron gauge reading, which records/measures the total hydrogen (non-condensables) derived from water according to the ideal gas law. Then, we calculated the water content (% H_2O), as a function of the amount of H_2 obtained and the sample weight (wt%). Long-term reproducibility for repeated determination of reference samples was better than ± 2‰ (1σ). Obtaining D/H values in phenocrysts (plagioclase, olivine, pyroxene) requires significant amount of gas released from melt/fluid inclusions (Table 1).

4. Results

4.1. Stable isotopes (δD, $\delta^{18}O$) and water content (H_2O wt%)

D/H ratios in glasses show a wide range of values, with δD spanning from −31.1 to −145.7‰ (Table 1). δD shows variations among the three eruptive stages at Deception Island, with post-caldera rocks generally presenting the heaviest δD (Table 1 and Fig. 5a). Pre-caldera glasses show the lightest D/H ratios, with δD ranging from −111.3 to 91.4‰. Syn-caldera glasses show slightly heavier D/H ratios (δD −83.4 to −91.2, ca. −87‰ on average) with exception of sample DI-31, which has the lightest value (−125.2‰). Post-caldera glasses present the largest δD range (−31.1 to −137.7‰), with most samples varying from −88.1 to −54.2‰. Extreme values correspond to samples DI-61 and DI-64 (−31.1 and −37.5‰, respectively) and to DI-39OBS and DI-4SUP (−137.7 and −109.8‰, respectively). Post-caldera samples mostly fall within the range of primary magmatic fluids (Fig. 5b, c), i.e. igneous waters, which derived from both direct measurements and indirect methods in volcanic systems (see e.g. Sheppard, 1977; Taylor Jr. and Sheppard, 1986; Hoefs, 2009 and references therein). Igneous water forms when magmas interact with meteoric waters and is slightly above and immediately below the isotopic composition of N-MORB mantle (−60‰; Clog et al., 2013) (Fig. 5c). By contrast to δD, $\delta^{18}O$ values in glasses are quite homogeneous ranging from to 4.5 to 6.2‰ within the normal values of basaltic rocks on Earth (≈3.5–7‰) (Bindeman, 2008). Water contents in glass (Fig. 6) mostly range from < 0.1 to 1.2 wt%, except for two samples that display values above 2 wt% (pre-caldera sample DI-18 and post-caldera sample DIPV37-F), with similar contents for pre-, *syn*- and post-caldera samples (Table 1).

Melt/fluid inclusions in plagioclase, olivine, pyroxene phenocrysts yielded low water contents of 0.1–0.5 wt% (Table 1; Fig. 6), and δD between −93.7 and −145.7‰. $\delta^{18}O$ in phenocrysts range between 5.0 and 6.0‰, and therefore, they are slightly higher than their host glasses

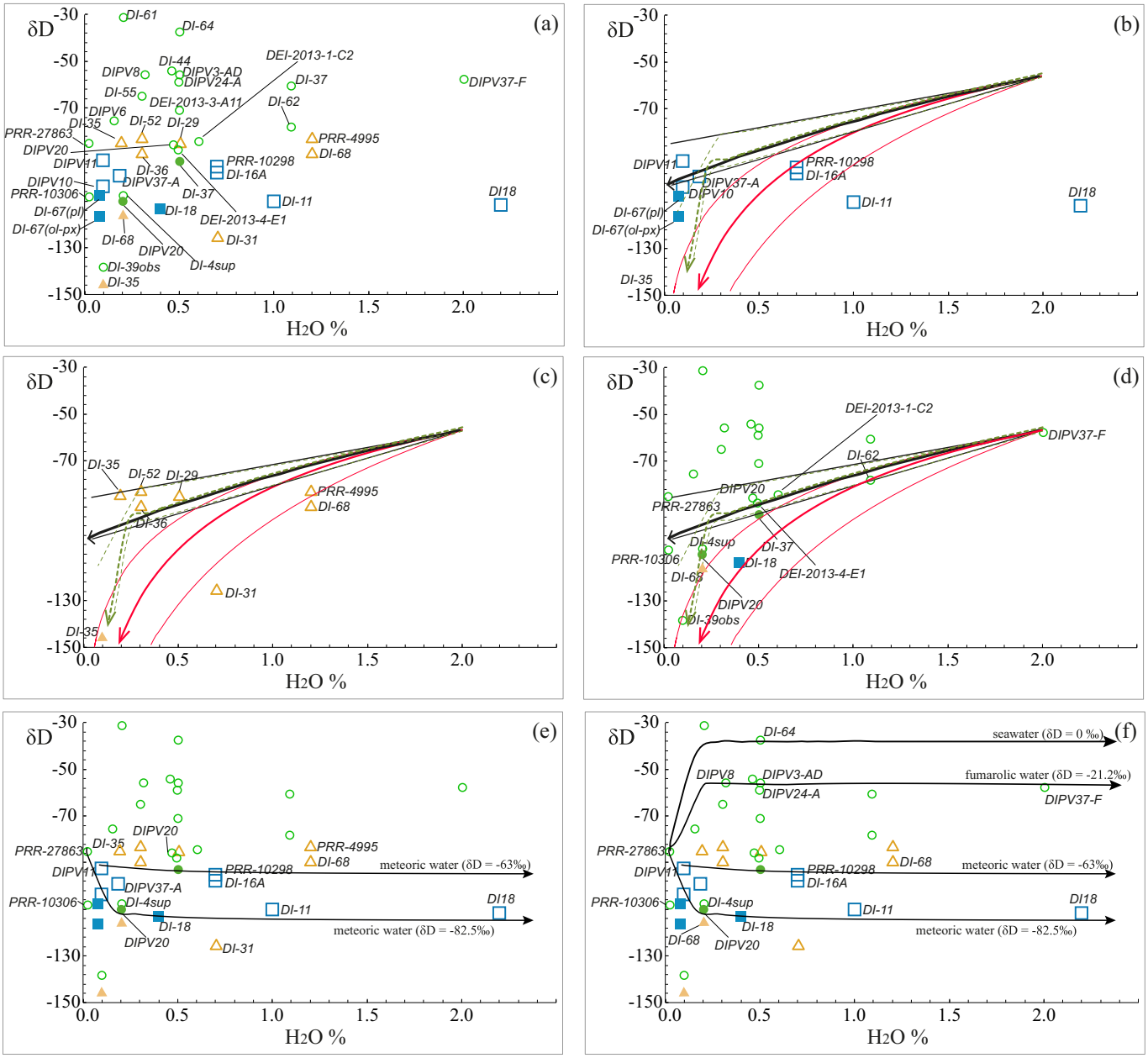

Fig. 6. (a) δD vs H_2O (%) diagram of the DI samples (symbols as in Fig. 5); Calculated degassing curves at closed- (red arrow), open- (black arrow) and mixed-system conditions (green dashed arrow), for the pre- (b), syn- (c) and post-caldera (d) samples. Water content variations from 1.5 to 2.5 wt% slightly change the curves slopes. Note in for instance that the path under closed system conditions shows the degassing connection among post-caldera samples (e.g. from DIPV37-F to PRR-27863). Lava sample e.g. DIPV10 displays slightly below the degassing curve at closed conditions. This suggests either a degassing mechanism at higher $\alpha_{melt\text{-}water}$ or degassing at closed conditions -up to very low water contents- followed by degassing at open conditions. In (b) the open-system degassing curve as in (a), remains backward in gray to highlight the common initial path with the mixed-system degassing curve; (e) (f) Calculated rehydration curves for pre- and syn-caldera samples, respectively. δD reference values of meteoric and fumarolic waters are from Kusakabe et al. (2009); In (e) for instance, the lightest meteoric water value (i.e. δD = −82.5‰) matches the values of e.g. sample DI-4SUP along the hydration trend. In (f) the rehydration curve between sample PRR-27863 and seawater (i.e. δD = 0‰) matches DI-64 sample, which is a sample collected next to the shore (Fig. 2). See the text for more details. (For interpretation of the references to colour in this figure legend, the reader is referred to the web version of this article.)

(Table 1, Fig. 5). Inclusions in phenocrysts generally show lower H_2O contents, lighter δD values, and slightly higher $\delta^{18}O$ than their host glass. DI-18 phenocryst and host glass, however, have nearly identical δD with contrasting water contents (0.4 wt% in phenocryst vs. 2.2 wt% in glass). By contrast, phenocryst and host glass in sample DI-35 show markedly different δD (−145.7 and −84.2‰ respectively) (Table 1, Figs. 5 and 6a).

4.2. Correlation among isotopic geochemistry, water sources and tectonics

Isotopic compositions of the studied samples change geographically, depending on the proximity to different external water sources (Figs. 1, 2). For instance, post-caldera samples with the heaviest D/H values, (e.g. DI-61, DI-64, DIPV6) were collected close to the coast and coastal thermal waters and fumaroles (Fig. 2); whereas the lightest D/H values belonging to the pre- and syn-caldera samples (e.g. DI-31, DI-35, DI-36) were collected away from the current coast line, near Mt. Kirkwood glacier (Fig. 1, Table 1). Kusakabe et al. (2009) reported δD and $\delta^{18}O$ of

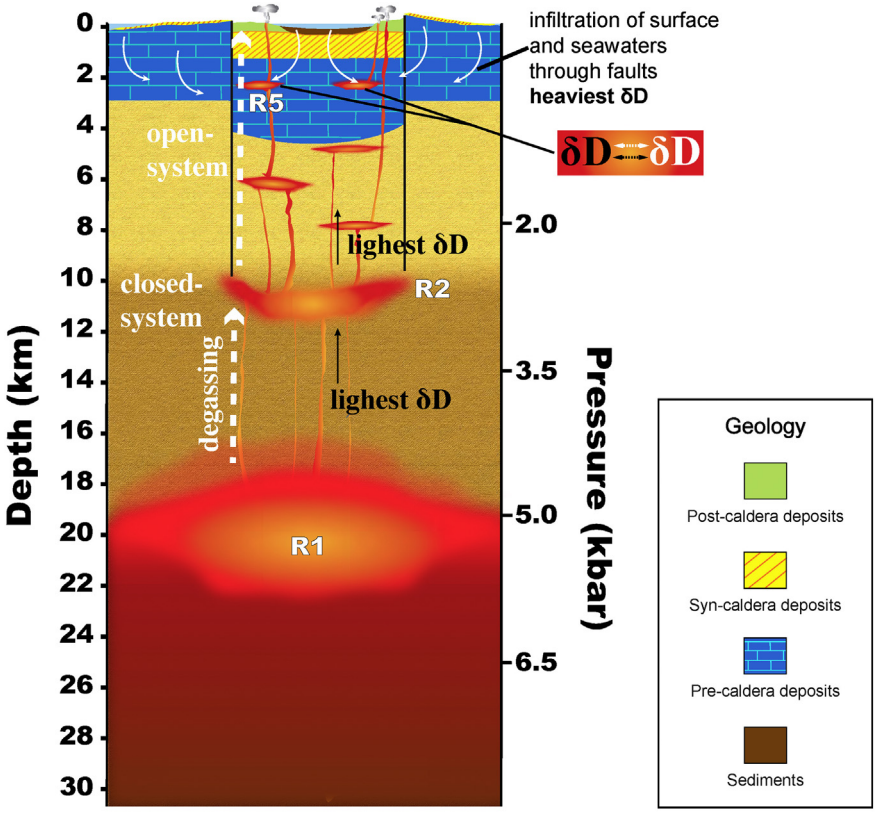

Fig. 7. Schematic summary of the isotopic variation at the post-caldera stage of Deception Island highlighting some sample examples under closed- vs. open- vs. mixed-system degassing conditions. Figure's background modified from Geyer et al. (2019). Early caldera formation stages are not portrayed (see Fig. 1). See details in the text.

surface waters (freshwater from crater lakes, ponds and glacier meltwater) in Deception Island (Fig. 5) ranging from −82 to −64‰ in D/H ratios and −10.9 to −7.8‰ in $\delta^{18}O$ (Fig. 5), as well as hot spring waters with values from close to seawater to local meteoric water (δD from −36.9 to −8.3‰, and $\delta^{18}O$ from −6.76 to −0.73). We utilized Kusakabe et al. (2009) results to compare δD values of our solid samples to the water values (Fig. 5) in order to understand potential pre-, syn- and post-eruptive interactions when magma ascends.

There is also an evident correlation between the measured isotopic ratios and the location of the Deception Island samples with respect to the two main fault systems. The post-caldera samples, with the heaviest D/H values, are mostly distributed along the NE-SW shallower structures described by De Rosa et al. (1995) (e.g. 1967, 1970 eruptions). The pre- and syn-caldera samples and few post-caldera samples (e.g. 1842 and 1969 eruptions) with the lightest D/H values follow the NW-SE trending deep fractures.

4.3. Degassing and rehydration calculations

We applied the equations of Newman et al. (1988) to the studied phenocrysts and glass samples to constrain the degassing and rehydration histories of the Deception Island magmas under closed, open, and mixed-systems conditions (Fig. 6). For degassing calculations, we input initial H_2O content of 2 wt% (Table 1), which is consistent with Geyer et al. (2019), and δD = −55‰ (Table 1) according to the N-MORB magmas (δD = −60 ± 5‰; Clog et al., 2013). See for instance post-caldera sample DIPV-37F with the highest water content. The heaviest δD value in the range of the N-MORB was used because of the slightly subduction-modified character of the Deception Island's mantle source (see Geyer et al., 2019). In addition, we considered no fractionation between residual melts during partial melting because of the high partial melting degree from the mantle source that produced these tholeiitic magmas (Bindeman et al., 2012; Geyer et al., 2019). Calculations were made at both constant and variable D/H fractionation factor between melt and water ($\alpha_{melt\text{-}water}$). The model of De Hoog et al. (2009) for basaltic melts was used to calculate variable $\alpha_{melt\text{-}water}$ values. For constant $\alpha_{melt\text{-}water}$ calculations two end-member values were used: (i) 1.03, 0.005 below the minimum value calculated by the De Hoog et al. (2009) model for a basalt with the given initial composition of 2 wt% H_2O and δD = −55‰; and (ii) 1.05 (rounded maximum value suggested for rhyolites by Newman et al., 1988 and Dobson et al., 1989). Potential effects of rehydration in the glass samples were calculated using the $\alpha_{glass\text{-}water}$ proposed by Friedman et al. (1993) for rhyolitic glass ($\alpha_{glass\text{-}water}$ = 0.9668 ± 5) (Fig. 6).

5. Discussion

5.1. Degassing and rehydration processes

Any volcanic glass, from silicic to mafic composition, is thermodynamically unstable at surface temperature and atmospheric pressure conditions, yet it can remain unaltered for millions of years at metastable conditions (Marshall, 1961). The first step of modification and alteration of fresh glass is rehydration by diffusion of the external water into the glass. The amount and rate of water incorporation into the glass strongly depends on numerous factors such as glass composition, ambient temperature, gradient of water concentration across the boundary, exposition time to water and pH (e.g. Anovitz et al., 2004; Seligman et al., 2016). Glass rehydration can start immediately after eruption during cooling and continues as long as the glass is exposed to the external water. Hydration may occur without producing mineralogical changes in volcanic glass (i.e. without formation of clay minerals, e.g. Kawano et al., 1993), as typically shown by rhyolitic glasses, which can hold up to 7 wt% H_2O in solution (Smith et al., 2001). On the other hand, rehydration and/or alteration of basaltic glass by interaction with external waters usually leads to the formation of an outer rind of palagonite with ~10 wt% water (e.g. Stroncik and Schmincke, 2002; Parruzot et al., 2015). In both cases, glass rehydration shows a hydration front containing a nanometer to micrometer thick layer of highly hydrated glass with 4–5 wt% H_2O that separates fresh and rehydrated

parts (e.g. Crovisier et al., 2003; Cailleteau et al., 2008; Valle et al., 2010; Seligman et al., 2016). Relevant to this study is the behaviour of H and O within the fresh and rehydrated glasses. δD ratios of glasses are traditionally considered to be controlled by the isotopic signal of external waters at the time of the rehydration and used as a proxy for paleoenvironmental reconstructions (Seligman et al., 2016). However, experiments on acid glasses by Anovitz et al. (2009) and Nolan and Bindeman (2013) showed that hydrogen atoms may be strongly mobile within glass at relatively low temperatures. Anovitz et al. (2009) demonstrated that in obsidian, at temperatures around 150 °C, magmatic hydrogen in the fresh glass isotopically exchanges and equilibrates with hydrogen in the rehydrated zones of the glass, which is a mixture of primary magmatic hydrogen and hydrogen incorporated by diffusion of external waters into the glass. In addition, Nolan and Bindeman (2013) showed isotopic exchange between hydrogen in glass and in external water in the scale of years at temperatures of 40 to 70 °C without involving further glass hydration. These experiments did not indicate significant interactions between oxygen in glass and external waters.

At Deception Island fast quenching and cooling of the pyroclastic deposits after eruption were enhanced by interaction with the existing ground- and surface water sources, including glaciers. This fast cooling potentially reduced the hydration and isotopic exchange, thus contributing to the preservation of original water contents and isotopic ratios in most rocks, especially for the younger post-caldera volcanoes.

Only the oldest samples (i.e. pre-caldera) show evidence of local alteration such as formation of secondary zeolites suggesting a significant period of glass exposed to external water (e.g. Fisher and Schmincke, 1984; Martí and Baraldo, 1990; Denton et al., 2009). However, even the highest measured water content in the island (pre-caldera glass sample DI-18 with c. 2.2%) is still under water saturation conditions of 3–4% H_2O (e.g. Anovitz et al., 2004; Giachetti et al., 2015; Seligman et al., 2016), thus supporting a low hydration process in the island. H_2O and δD values of many glasses indicate negligible rehydration. For instance, the water-poor obsidian sample DI-39OBS contains < 0.1% H_2O, as expected for the typical low water solubility in high temperature cooling lavas (Friedman and Smith, 1958; Newman and Lowenstern, 2002).

Our calculations for degassing and rehydration in the Deception Island samples show that isotopic ratios and water contents of magmas with an initial δD value close to −55‰, are consistent with degassing en-route to the surface in either a closed-, or open-, or mixed-systems, and with the subsequent rehydration of the emitted materials (Fig. 6).

Most samples display δD isotopic values in the range of closed- and open-system degassing (Fig. 6a). Those samples outside this range correspond to the post-caldera with the heaviest δD values and < 0.5 wt % H_2O, as well as the pre- and *syn*-caldera samples with the lightest δD values and > 0.75 wt% H_2O. The glass data show minor variation in $\delta^{18}O$, pointing to a limited fractionation between melt and water vapor that leaves the magma at high temperature, as even complete degassing yields to negligible $\delta^{18}O$ shift (see also Bindeman, 2008). Moreover, there are no low-$\delta^{18}O$ signatures (i.e. below 4.5‰) that would indicate extensive (given the higher O content in glass this element is less sensitive to isotopic composition changes compared to H) interactions of stagnant magma at depth with meteoric or seawaters prior to eruption. This implies that (i) phreatomagmatic and magmatic eruptions were fed by magma sources deeper than c. 10 km (see also Geyer et al., 2019) where infiltration of surficial water is strongly limited, and (ii) the low porosity of the rock samples did not allow low-$\delta^{18}O$ waters to circulate (e.g. Taylor Jr. and Sheppard, 1986). Therefore, deviations from the expected degassing trends (Fig. 6b, c, d) are most likely related to post-emplacement rehydration (i.e. by surface weathering and/or hydrothermal alteration) of glass by seawater and meteoric waters of variable δD values (Fig. 6e, f).

The most poorly or unhydrated glasses indicating rapid magma ascent and quenching during eruption fall along the closed-system degassing trend (Fig. 6b, c, d). This indicates rapid magma ascent and quenching during eruption which preserved the magmatic isotopic ratios (e.g. see Hallis et al., 2015). This observation is consistent with explosive eruptions being produced by magmas evolving and degassing in closed-system conditions leading to pressure build-up (Newman et al., 1988; Dobson et al., 1989). Magma ascent and quenching during eruption was fast enough to inhibit further degassing of glass in the pyroclasts (see also Taylor et al., 1983). Current degassing of Deception Island magmas in a closed-system scenario is also supported by the negligible contribution of primary magmatic component into the fumarolic gas and hot spring waters in the island (Kusakabe et al., 2009), despite the shallow depth of the most recently formed magma reservoirs (Geyer et al., 2019). Fast ascent and quenching of magmas during explosive phreatomagmatic eruptions in Deception Island is also supported by petrography of the pyroclastic samples (Pedrazzi et al., 2018; Geyer et al., 2019).

In contrast to the pyroclasts, the lava samples shift towards an open-system degassing model. This is coherent with the open system degassing of magmas leading to effusive eruptions proposed by Newman et al. (1988) and Dobson et al. (1989). Open-system degassing can also occur at depth if an initial explosive event opens the feeder dyke systems, yielding a mixed-system degassing in the cooling lavas. Therefore, the preservation of isotope signature of the magmatic source, combined with absence of significant interaction of magmas with external waters (i.e. isotope exchange), allows us to infer the original isotopic ratios of the magma source itself.

5.2. Constraining magma source

The magmas at Deception Island have a tholeiitic character (Geyer et al., 2019) that indicates high partial melting degree (> 10–15%), which produced the negligible D/H isotopic fractionation among the successive residual and/or mixing glass generations during melting (Bindeman et al., 2012). This can ensure a mantle isotopic signature in newly formed magmas. The initial δD of Deception Island magmas matches the range of other magmatic sources considered as existing D/H keepers, such as Koolau and Baffin Island magmas (Hallis et al., 2015), and within the range (δD = −60 ± 5‰) of the N-MORB mantle (Clog et al., 2013). This observation supports the model by Geyer et al. (2019) proposing a N-MORB mantle slightly modified by prior subduction as a source of magmas in Deception Island. Water contribution from the subducting slab may have induced a minor modification of the δD values of the original N-MORB mantle wedge towards heavier δD values (e.g. Giggenbach, 1992), such as −55‰ or even heavier.

5.3. Shallow-depth magmatic processes

5.3.1. Pre-caldera stage

Pyroclastic samples match degassing at closed-system conditions, whereas lava samples likely indicate a mixed mode of degassing (Fig. 6b, c, d). DIPV10 lava sample displays, however, similarities with the calculated closed-system degassing curves. This is consistent with either (i) closed system degassing with slightly higher $\alpha_{melt\text{-}water}$ (> 0.9668) or (ii) most likely minor late stage open-system degassing (at depth following the opening and/or during ascent and emplacement) after dominant closed-system degassing. The initial degassing precluding the eruptions that formed the pre-caldera Deception volcano. These older deposits have been affected by variable magma's rehydration from meteoric waters, which in turn is in agreement with the reconstructed pre-caldera's topography in conical shape hat hindered access of sea water in the central part of Deception Island (Torrecillas et al., 2013).

Rehydration of glass sample DIPV11-B by meteoric waters (δD = −63‰, Kusakabe et al., 2009) may lead to glass values of D/H such as of samples DI-16A and PRR-10298 (Fig. 6c). Similar values to those of samples DI-11 and DI-18 (including the phenocryst) can be

obtained by rehydration of the same initial glass with meteoric waters with lower δD values (i.e. δD = −82.5‰, Kusakabe et al., 2009). Sample DIPV37-A accounts for intermediate δD water values (Fig. 6c). D/H ratio and water content of melt inclusions in the DI-18 phenocryst are compatible with minor rehydration, thus suggesting that this particular phenocryst may keep the original magmatic value without influence of external waters.

5.3.2. Syn-caldera stage

Glasses in pyroclasts are consistent with magma degassing in closed-system conditions followed by rehydration of meteoric waters (Fig. 6c). The meteoric origin of the rehydration water is consistent with their sampling location significantly above the current sea level. In addition, it may also indicate that eruption, deposition and cooling of the *syn*-caldera ignimbrites occurred prior to caldera inundation by the sea.

Rehydration of sample DI-35 by the heaviest meteoric water (δD = −63‰, Kusakabe et al., 2009), can produce compositions similar to those of other syn-caldera samples (e.g. DI-68, Fig. 6c). However, other samples, e.g. PRR-4995 displays above the rehydration curve (Fig. 6c), suggesting rehydration of an initially less degassed glass. The formation of the voluminous Outer Coast Tuff Formation ignimbrite involved large magma reservoirs, which can present heterogeneous degassing histories and wide range of magma composition. The fast emptying of these magma reservoirs (Geyer et al., 2019) precludes significant mixing and homogenization of magmas and hampers its further degassing. In consequence, emission of variably degassed magmas is expected. These should display along a closed-system degassing curve (Taylor et al., 1983), providing different starting points for rehydration curves.

Phenocrysts of samples DI-35 and DI-68 show significantly lighter δD values than their host glasses, within the range of open-system degassing curves (Fig. 6b, c). This may imply that these crystals formed in a further open-system degassed magma, thus indicating either addition of crystals from previously crystallized magmas or cumulates into the new magma, or magma mixing. On the other hand, sample DI-31 presents values below the open-system degassing curve which cannot be reached by rehydration of a glass like DI-35 by meteoric waters with δD much lower than the range given in Kusakabe et al. (2009); i.e. δD as light as −110‰ would be needed.

According to the pressure estimates by Geyer et al. (2019) of the two different magma reservoirs existing under Deception Island at the time of the caldera eruption (i.e. R1 and R2 which were emplaced at progressively shallower depths, Fig. 7), glasses DI-31 and DI-68 became equilibrated at shallower depths (c. 10 km, R2) than most of the syn-caldera samples (c. 14–20 km, R1). Therefore, our isotopic results confirm the simultaneous presence of two reservoirs at different depths fed by nearly identical magmas (evidenced by the main compositional cluster of the *syn*-caldera samples in Geyer et al., 2019), and degassing under different conditions: i.e. open-system in R2, and closed-system in the deeper reservoir (i.e. R1). Geyer et al. (2019) proposed that the deepest reservoir, R1, would be the first to form and larger one, with the smaller reservoir R2 enlarging by the magma ascent from R1. This model (Fig. 7) is consistent with our isotopic data: i.e. magmas in deep R1 would have degassed in closed-system conditions, whereas those ascending to the shallower R2 would have experienced a second stage of open-system degassing. Magmas in R2 show slightly more evolved compositions than the ones in R1, which may indicate (i) tapping of the evolved regions in a slightly heterogeneous R1; (ii) minor differentiation during ascent and stagnation at R2; (iii) late minor mafic magma contribution to R1. In any case, little chemical differentiation of magmas in R2 compared to those in R1 suggests short life of R2 prior to eruption. Hence, volatiles rich R1 magma ascended through R2, incorporating, and partially mingling its degassed magmas. This mingling may be responsible for the presence of mixed glass populations observed in some *syn*-caldera samples (Geyer et al., 2019), and can explain the presence of open-system phenocrysts within closed-system samples.

5.3.3. Post-caldera stage

Water content and isotopic ratios of the post-caldera deposits show the widest range of values among all samples. The dominant setting corresponds to closed-system degassing and post-eruptive rehydration by surface waters (i.e. oceanic, fumarolic, meteoric/glacier-meltwater) (Fig. 6a, d, f). Samples along the closed-system degassing trend (e.g. from DIPV37-F to PRR-10306) may represent magmas erupted at different degassing conditions (Newman et al., 1988), and be directly correlated to their reservoir location at depth. Glass data from the PRR-27863 sample, for instance, can match most samples through the calculated rehydration path (Fig. 6d) depending on the considered water source: i.e. seawater (δD = 0‰; e.g. DI-64), fumarolic water (δD = −8 to −21.2‰, Kusakabe et al., 2009; e.g. DI-44 and DIPV37-F), or meteoric water (δD = −63 to −82.5‰, Kusakabe et al., 2009; e.g. DI-4SUP). Hydrogen isotope ratio of sample DI-61 (δD = c. −34‰) is above the maximum δD of rhyolitic volcanic glass in equilibrium with seawater if we use $\alpha_{glass\text{-}water}$ by Friedman et al. (1993). This indicates that seawater may interact in this sample at the time of the eruption, not by dissolution mechanisms at depth, but by kinetic factors affecting the rock minerals and glass such as local seawater variations in salinity, pH or Eh.

On the other hand, obsidian sample DI-39OBS shows evidences of open-system degassing from erupting magma that is considered to have resided at a shallow reservoir (c. 2 km). This sample texturally shows a transition from vesicular pumice to massive obsidian, which evidences variable degassing stages. This suggests that magma solidified at different parts of the shallow magma plumbing system (e.g. feeder dyke margin vs dyke core), which was later excavated by explosive eruptions (Newman et al., 1988). We interpret such variation of textures as a heterogeneously degassed magma reservoir, where the obsidian clasts (DI-39OBS) may represent the most heavily degassed regions of the reservoir. Its degassing trend (Fig. 6d) is consistent with an initial closed-system followed by open-system degassing. For a lava flow (e.g. sample PRR-27863), this setting could represent the latest degassing stage (Newman et al., 1988; Dobson et al., 1989). We suggest that the open-system trend was produced by migration of volatiles within the closed magma reservoir. Volatile migration in a closed-system may favour δD enrichment in the areas of gas accumulation where host melts will have δD heavier than expected for a closed-system degassing setting (e.g. heavy δD in sample PRR-27863). Sample DI-4SUP can be interpreted as either the result of a mixed-system degassing as for DI-39OBS, or due to rehydration of a glass like PRR-27863 by the lightest meteoric water during eruption.

Phenocryst DIPV20 shows a more degassed evolution than its host DIPV20 vesiculated lava (Fig. 6a) that has the highest water content of 0.5%, a typical value for a lava flow, thus secondary hydration cannot be ruled out. If phenocryst DIPV20 is assumed to record pre-eruptive conditions at depth, its location at the upper part of the open-system degassing curve, as well as its closeness to the mixed-system degassing curve, supports open-system degassing during the post-caldera stage.

Sample DI-37 with a thermodynamically estimated water content of c. 0.5–0.75 wt% (Geyer et al., 2019) is one of the most basic rocks studied in Deception Island and indicates a deep pre-eruptive origin (> 30 km). These conditions match our measured D/H and water content, as a plausible original trapped melt in phenocryst DI-37 after minor open-system degassing (Fig. 7).

5.4. Linking magma compositions and isotopic geochemistry with active tectonics

We found a broad correlation between isotopic ratios (Table 1) and location of volcanoes regarding the two main fault systems in the island (Fig. 1), which may control the paths for ascending magmas. For the post-caldera samples, the shallow NE-SW trending faults correlate to

the eruption of the most evolved magmas (e.g. 1967, 1970 eruptions) (Table 1; see also De Rosa et al., 1995; Geyer et al., 2019). Geobarometric estimates (Geyer et al., 2019) indicate shallow depths of magma sources (e.g. c. 2 km in Cross-Hill), which suggest that magma favoured ascent through NE-SW faults (e.g. Holland et al., 2011; Schipper et al., 2013). Hence, the D/H values and the faults depth are compatible and coherent with the lithostatic pressure (P) estimates for the post-caldera (≈2–15 km) and pre-*syn*-caldera samples (≈6–35 km), which were retrieved through thermodynamic modelling in the same samples (Table 1; see also Geyer et al., 2019). Shallow faults, among other key geological features, such as shallow soft-sediment cover, topography and proximity to seawater, can strongly influence eruption styles in monogenetic volcanoes (Kereszturi et al., 2017). At Deception Island, a similar set of factors may have influenced magma-water interactions, resulting in Surtseyan style and phreatomagmatic eruptions (Pedrazzi et al., 2018; Geyer et al., 2019).

This geographical correlation is also observable in the pre- and syn-caldera deposits, i.e. deeper NW-SE trending faults broadly correlate to magmas with the lightest D/H values revealing negligible or null interaction at depth with waters from surface. However, since the post-caldera deposits currently cover the pre- and syn-caldera emission vents, this requires further research to untangle such correlations for the pre- and syn-caldera deposits (Fig. 2).

5.5. Implications for hazard assessment and eruption forecasting

A key point in planning for volcanic hazards is to find an unknown location of the next vent. Recent multidisciplinary geological studies have notably advanced pre-eruption preparedness and hazard assessment for society (e.g. Albert et al., 2016; Kereszturi et al., 2017). Our isotopic results indicate that the magmatic system beneath Deception Island is currently dominated by closed-system degassing, capable to promote both magmatic and phreatomagmatic eruptions. Magma explosiveness in future eruptions in the island will be constrained by magma ascent conditions (controlled by ascent rate, composition, vesicularity, among others), as well as shallow interactions with surface water and groundwater. The two cases depend, to some extent, on the active faults. Therefore, tectonic control on eruption triggering must be also considered in Deception Island (e.g. Darwin, 1840; Nakamura, 1975; Linde and Sacks, 1998). We claim for monitoring of a volcanic activity that combines seismics (e.g. faults reactivation) with other techniques, such as geochemical studies of volatiles to obtain information on forecasting a future volcanic eruption (e.g. Hernández et al., 2001; Aiuppa et al., 2006; Sano et al., 2015). It has been reported that the 2011 eruption of El Hierro submarine volcano started release of noble gases from depth (i.e. eruption's triggering) several weeks before the beginning of the seismic activity (Padrón et al., 2013; Álvarez-Valero et al., 2018). In addition, the studies of the syn-caldera eruption stages are required to understand the possible coexistence of contemporary open- and closed-system reservoirs at different depths for an accurate assessment of future eruptions.

6. Conclusions

- The fast ascent of magmas leading to the eruptive events at Deception Island are revealed by (i) the low to negligible secondary hydration in the pre- and post-caldera samples, respectively; and (ii) the insignificant contribution of magmatic waters into the fumarolic gas and hot spring water samples in the island (Kusakabe et al., 2009).
- Magmas feeding Deception Island eruptions (including the shallowest reservoirs) came from deep source (c. > 10 km) where meteoric/oceanic waters had no access to contact them. This is also evidenced by the negligible variations in the oxygen isotope values respect to their magmatic signatures, indicating isotope exchange associated with hydrovolcanism after magma-water interactions, and/or at the shallowest reservoirs in which meteoric and seawaters might have infiltrated through crustal faults.
- Our study demonstrates that geochemistry of stable isotopes is the complementary tool of the entire petrological information, to advance in the knowledge of magmas degassing and potential rehydration processes in an active hydrovolcanic system.

Declaration of competing interest

The authors declare that they have no known competing financial interests or personal relationships that could have appeared to influence the work reported in this paper.

Acknowledgements

This research was supported by the Spanish Government (MINECO projects) RECALDEC (CTM2009-05919-E/ANT), PEVOLDEC (CTM2011-13578-E/ANT), POSVOLDEC (CTM2016-79617-P)(AEI/FEDER, UE), VOLGASDEC (PGC2018-095693-B-I00)(AEI/FEDER, UE), and USAL-2019 project (Programa Propio - mod. 1B). A.G. is grateful for her Ramón y Cajal contract (RYC-2012-11024). We thank all the military staff of the Spanish Antarctic Base “Gabriel de Castilla” for their constant help and logistic support, and the crew of the scientific vessel “BIO-Hespérides” without which this research would not have been possible. We very much appreciate the careful and in-depth reviews by Minoru Kusakabe and editor. We also thank the Polar Rock Repository (http://research.bpcrc.osu.edu/rr/) for loaning the rock samples PRR-10298, PRR-10306, PRR-27863 collected by C.H. Shultz in 1970, and PRR-4995 by Pamela J. Ellerman Lundstrom in 1984. This research is also included in POLARCSIC activities.

References

Abràmoff, M.D., Magalhães, P.J., Ram, S.J., 2004. Image processing with ImageJ. Biophotonics International 11, 36–42.
Aiuppa, A., Federico, C., Giudice, G., Gurrieri, S., Liuzzo, M., Shinohara, H., Favara, R., Valenza, M., 2006. Rates of carbon dioxide plume degassing from Mount Etna volcano. J. Geophys. Res. Solid Earth 111.
Albert, H., Costa, F., Martí, J., 2016. Years to weeks of seismic unrest and magmatic intrusions precede monogenetic eruptions. Geology 44, 211–214.
Almendros, J., Carmona, E., Jiménez, V., Díaz-Moreno, A., Lorenzo, F., 2015. Volcano-tectonic activity at Deception Island volcano following a seismic swarm in the Bransfield Rift (2014–2015). Geophys. Res. Lett. 45, 4788–4798.
Álvarez-Valero, A.M., Burgess, R., Recio, C., de Matos, V., Sánchez-Guillamón, O., Gómez-Ballesteros, M., Recio, G., Fraile-Nuezc, E., Sumino, H., Flores, J.A., Ban, M., Geyer, A., Bárcenas, M.A., Borrajo, J., Compaña, J.M., 2018. Noble gas signals in corals predict submarine volcanic eruptions. Chem. Geol. 480, 28–34.
Anovitz, L.M., Elam, J.M., Riciputi, L.R., Cole, D.R., 2004. Isothermal time series determination of the rate of diffusion of water in Pachuca obsidian. Archaeometry 46, 301–326.
Anovitz, L.M., Cole, D.R., Riciputi, L.R., 2009. Low temperatura isotopic exchange in obsidian: implications for diffusive mechanisms. Geochim. Cosmochim. Acta 73, 3795–3806.
Antoniades, D., Giralt, S., Geyer, A., Álvarez-Valero, A.M., Pla-Rabes, S., Granados, I., Liu, E.J., Smellie, J.L., Oliva, M., 2018. The timing and widespread effects of the largest Holocene volcanic eruption in Antarctica. Sci. Rep. 8 (1), 17279.
Aparicio, A., Menegatti, N., Petrinovic, I., Risso, C., Viramonte, J.G., 1997. El volcanismo de Isla Decepción (Península Antártida). Bol. Geol. Min. 108, 235–258.
Baker, P.E., McReath, I., Harvey, M.R., Roobol, M.J., Davies, T.G., 1975. The geology of the south Shetland islands: Volcanic evolution of Deception island. BAS Sci. Rep. 78 (81pp).
Barclay, A.H., Wilcock, W.S.D., Ibáñez, J.M., 2009. Bathymetric constraints on the tectonic and volcanic evolution of Deception Island Volcano, South Shetland Islands. Antarct. Sci. 21 (2), 153–167.
Bartolini, S., Geyer, A., Martí, J., Pedrazzi, D., Aguirre-Díaz, G., 2014. Volcanic hazard on Deception Island (South Shetland Islands, Antarctica). J. Volcanol. Geotherm. Res. 285, 150–168.
Bigeleisen, J., Perlman, M.L., Prosser, H.C., 1952. Conversion of hydrogenic materials to hydrogen for isotopic analysis. Anal. Chem. 24, 1536–1537.
Bindeman, I., 2008. Oxygen isotopes in mantle and crustal magmas as revealed by single crystal analysis. Rev. Mineral. Geochem. 69, 445–478.
Bindeman, I.N., Kamenetsky, V.S., Palandri, J., Vennemann, T., 2012. Hydrogen and oxygen isotope behaviors during variable degrees of upper mantle melting: example from the basaltic glasses from Macquarie Island. Chem. Geol. 310-311, 126–136.
Birkenmajer, K., 1992. Evolution of the Bransfield Basin and rift, West Antarctica, in

Recent Progress in Antarctic Earth Sciences. In: Yoshida, Y., Kaminuma, K., Shiraishi, K. (Eds.), Terra Scientific Publishing Company, pp. 405–410.
Birkenmajer, K., Soliani, E., Kawashita, K., 1990. Reliability of potassium-argon dating of Cretaceous-Tertiary island-arc volcanic suites of King George Island, South Shetland Islands (West Antarctica). Zentral. Geol. Palaönt. 1, 127–140.
Borthwick, J., Harmon, R.S., 1982. A note regarding ClF_3 as an alternative to BrF5 for oxygen isotope analysis. Geochim. Cosmochim. Acta 46, 1665–1668.
Cailleteau, C., Angeli, F., Devreux, F., Gin, S., Jestin, J., Jollivet, P., Spalla, O., 2008. Insight into silicate-glass corrosion mechanisms. Nat. Mater. 7, 978–983.
Cashman, K., Mangan, M., 1994. Physical aspects of magmatic degassing. In: Carroll, M., Holloway, J. (Eds.), Volatiles in Magmas—Reviews in Mineralogy. Mineralogical Society of America, Chantilly, pp. 447–478.
Catalán, M., Galindo-Zaldivar, J., Martín-Davila, J., Martos, Y.M., Maldonado, A., Gamboa, L., Schreider, A.A., 2013. Initial stages of oceanic spreading in the Bransfield Rift from magnetic and gravity data analysis. Tectonophysics 585, 102–112.
Catalán, M., Martos, Y.M., Galindo-Zaldívar, J., Funaki, M., 2014. Monitoring the evolution of Deception Island volcano from magnetic anomaly data (South Shetland Islands, Antarctica). Glob. Planet. Chang. 123 (Part B), 199–212.
Clayton, R.N., Mayeda, T.K., 1963. The use of bromine pentafluoride in the extraction of oxygen from oxides and silicates for isotopic analysis. Geochim. Cosmochim. Acta 27, 43–52.
Clog, M., Aubaud, C., Cartigny, P., Dosso, L., 2013. The hydrogen isotopic composition and water content of southern Pacific MORB: areassessment of the D/H ratio of the depleted mantle reservoir. Earth Planet. Sci. Lett. 381, 156–165.
Correig, A.M., Urquizu, M., Gila, J., Marti, J., 1997. Analysis of the temporal occurrence of seismicity at Deception Island (Antarctica). Pure Appl. Geophys. 149, 553–574.
Crovisier, J., Advocat, T., Dussossoy, J., 2003. Nature and role of natural alteration gels formed on the surface of ancient volcanic glasses (Natural analogs of waste containment glasses). J. Nucl. Mater. 321, 91–109.
Darwin, C., 1840. On the connexion of certain volcanic phenomena in South America; and on the formation of mountain chains and volcanoes, as the effect of the same power by which continents are elevated. Trans. Geol. Soc. Lond. 5, 601–631.
De Hoog, C.J., Taylor, B.E., Van Bergen, M.J., 2009. Hydrogen-isotope systematics in degassing basaltic magma and application to Indonesian arc basalts. Chem. Geol. 266, 256–266.
De Rosa, R., Mazzuoli, R., Omarini, R., Ventura, G., Viramonte, J., 1995. A volcanological model for the historical eruptions at Deception Island, Bransfield Strait, Antarctica. Terra Antarct. 2, 95–101.
DeGroat-Nelson, P.J., Cameron, B.I., Fink, J.H., Holloway, J.R., 2001. Hydrogen isotope analysis of rehydrated siclic lavas: implications for eruption mechanisms. Earth Planet. Sci. Lett. 185, 331–341.
Delmas, R.J., Kirchner, S., Palais, J.M., Petit, J.R., 1992. 1000 years of explosive volcanism recorded at the South Pole. Tellus Ser. B Chem. Phys. Meteorol. 44, 335–350.
Denton, J.S., Tuffen, H., Gilbert, J.S., Odling, N., 2009. The hydration and alteration of perlite and rhyolite. J. Geol. Soc. 166, 895–904.
Dobson, P.F., Epstein, S., Stolper, E.M., 1989. Hydrogen isotope fractionation between coexisting vapour and silicate glasses and melts at low pressure. Geochim. Cosmochim. Acta 53, 2723–2730.
Fisher, R.V., Schmincke, H.-U., 1984. Alteration of volcanic glass. In: Fisher, R.V., Schmincke, H.-U. (Eds.), Pyroclastic Rocks. Springer, Berlin, pp. 312–345.
Fretzdorff, S., Smellie, J.L., 2002. Electron microprobe characterization of ash layers in sediments from the central Bransfield basin (Antarctic Peninsula): evidence for at least two volcanic sources. Antarct. Sci. 14, 412–421.
Friedman, I., Smith, R.L., 1958. The deuterium content of water in some volcanic glasses. Geochim. Cosmochim. Acta 15, 218–228.
Friedman, I., Gleason, J., Sheppard, R.A., Gude, A.J., 1993. Deuterium fractionation as water diffuses into silicic volcanic ash. AGU Geophys. Monogr. 78, 321–323.
Geyer, A., Martí, J., 2008. The new worldwide collapse caldera database (CCDB): a tool for studying and understanding caldera processes. J. Volcanol. Geotherm. Res. 175, 334–354.
Geyer, A., Álvarez-Valero, A.M., Gisbert, G., Aulinas, M., Hernández-Barreña, D., Lobo, A., Marti, J., 2019. Deciphering the evolution of the Deceptions Island's magmàtic system. Sci. Rep. 9, 373.
Giachetti, T., Gonnermann, H.M., Gardner, J.E., Shea, T., Gouldstone, A., 2015. Discriminating secondary from magmatic water in rhyolitic matrix-glass of volcanic pyroclasts using thermogravimetric analysis. Geochim. Cosmochim. Acta 148, 457–476.
Giggenbach, W.F., 1992. Isotopic shifts in waters from geothermal and volcanic systems along convergent plate boundaries and their origin. Earth Planet. Sci. Lett. 113, 495–510.
Godfrey, J.D., 1962. The deuterium content of hydrous minerals from the east-Central Sierra Nevada and Yosemite National Park. Geochim. Cosmochim. Acta 26, 1215–1245.
González-Ferrán, O., 1985. Volcanic and tectonic evolutionof the northern Antarctic Peninsula-late Cenozoic to recent. Tectonophysics 114, 389–409 (1985).
Grad, M., Guterch, A., Sroda, P., 1992. Upper crustal structure of Deception Island area, Bransfield Strait, West Antarctica. Antarct. Sci. 4, 469–476.
Haase, K.M., Beier, C., Fretzdorff, S., Smellie, J.L., Garbe-Schönberg, D., 2012. Magmatic evolution of the South Shetland Islands, Antarctica, and implications for continental crust formation. Contrib. Mineral. Petrol. 163, 1103–1119.
Hallis, L.J., Huss, G.R., Nagashima, K., Taylor, J., Halldórsson, S.A., Hilton, D.R., Mottl, M.J., Meech, K.J., 2015. Evidence for primordial water in Earth's deep mantle. Science 350 (6262), 795–797.
Hernández, P.A., Notsu, K., Salazar, J.M., Mori, T., Natale, G., Okada, H., Virgili, G., Shimoike, Y., Sato, M., Pérez, N.M., 2001. Carbon dioxide degassing by advective flow from Usu Volcano, Japan. Science 292, 83–86.
Hoefs, J., 2009. Stable Isotope Geochemistry, 6th ed. Springer-Verlag Berlin Heidelberg (285 pp).
Hole, M.J., Saunders, A.D., Rogers, G., Sykes, M.A., 1994. The relationship between alkaline magmatism, lithospheric extension and slab window formation along continental destructive plate margins. Geol. Soc. Lond., Spec. Publ. 81, 265–285.
Holland, A.S.P., Watson, I.M., Phillips, J.C., Caricchi, L., Dalton, M.P., 2011. Degassing processes during lava dome growth: Insights from Santiaguito lava dome, Guatemala. J. Volcanol. Geotherm. Res. 202, 153–166.
Ibáñez, J.M., Del Pezzo, E., Almendros, J., La Rocca, M., Alguacil, G., Ortiz, R., García, A., 2000. Seismovolcanic signals at Deception Island volcano, Antarctica: wave field analysis and source modelin. J. Geophys. Res. Solid Earth 105 (6), 13905–13931.
Ibáñez, J.M., Almendros, J., Carmona, E., Martínez-Arévalo, C., Abril, M., 2003. The recent seismo-volcanic activity at Deception Island volcano. Deep-Sea Res. II Top. Stud. Oceanogr. 50, 1611–1629.
Ibáñez, J.M., Díaz-Moreno, A., Prudencio, J., Zandomeneghi, D., Wilcock, W., Barclay, A., Almendros, J., Benítez, C., García-Yeguas, A., Alguacil, G., 2017. Database of multiparametric geophysical data from the TOMO-DEC experiment on Deception Island, Antarctica. Sci. Data 4, 170128.
Jambon, A., Zimmermann, J.L., 1990. Water in oceanic basalts: evidence for dehydration of recycled crust. Earth Planet. Sci. Lett. 101 (2–4), 323–331.
Jenkin, G.R.T., 1988. Stable Isotope Studies in Caledonides of SW Connemara, Ireland. PhD thesis. Univ. Glasgow, UK.
Kawano, M., Tomita, K., Kamino, Y., 1993. Formation of clays minerals during low-temperature experimental alteration of obsidian. Clay Clay Miner. 41, 431–441.
Kereszturi, G., Bebbington, M., Németh, K., 2017. Forecasting transitions in monogenetic eruptions using the geologic record. Geology 45, 283–286.
Košler, J., Magna, T., Mlcoch, B., Mixa, P., Nývlt, D., Holub, F., 2009. Combined Sr, Nd, Pb and Li isotope geochemistry of alkaline lavas from northern James Ross Island (Antarctic Peninsula) and implications for back-arc magma formation. Chem. Geol. 258, 207–218.
Kraus, S., Kurbatov, A., Yates, M., 2013. Geochemical signatures of tephras from Quaternary Antarctic Peninsula volcanoes. Andean Geol. 40, 1–40.
Kusakabe, M., Ohwada, M., Satake, H., Nagao, K., Kawasaki, I.R., 2003. Helium isotopic ratios and geochemistry of volcanic fluids from the Norikura Volcanic Chain, Central Japan: implications for crustal structures and seismicity. Geochim. Cosmochim. Acta 67 (18), 243.
Kusakabe, M., Nagao, K., Ohba, T., Seo, J.H., Park, S.-H., Lee, J.I., Park, B.-K., 2009. Noble gas and stable isotope geochemistry of thermal fluids from Deception Island, Antarctica. Antarct. Sci. 21, 255–267.
Lange, R.A., 1994. The effect of H_2O, CO_2 and F on the density and viscosity of silicate melts. Rev. Mineral. 30, 331–369.
Le Bas, M.J., Le Maitre, R.W., Streckeisen, A., Zanettin, B.A., 1986. Chemical classification of volcanic rocks based on the total alkali-silica diagram. J. Petrol. 27, 745–750.
Linde, A.T., Sacks, I.S., 1998. Triggering of volcanic eruptions. Nature 395, 888–890.
Luzón, F., Almendros, J., García-Jerez, A., 2011. Shallow structure of Deception Island, Antarctica, from correlations of ambient seismic noise on a set of dense seismic arrays. Geophys. J. Int. 185, 737–748.
Marshall, B.R., 1961. Devitrification on natural glass. Geol. Soc. Am. Bull. 72, 1493–1520.
Martí, J., Baraldo, A., 1990. Pre-caldera pyroclastic deposits of Deception Island (South Shetland Islands). Antarct. Sci. 2, 345–352.
Martí, J., Geyer, A., Aguirre-Diaz, G., 2013. Origin and evolution of the Deception Island caldera (South Shetland Islands, Antarctica). Bull. Volcanol. 75, 1–18.
Middlemost, E.A.K., 1989. Iron oxidation ratios, norms and the classification of volcanic rocks. Chem. Geol. 77, 19–26.
Moreton, S.G., Smellie, J.L., 1998. Identification and correlation of distal tephra layers in deep-sea sediment cores, Scotia Sea, Antarctica. Ann. Glaciol. 27, 285–289.
Nakamura, K., 1975. Volcano structure and possible mechanical correlation between volcanic eruptions and earthquakes. Bull. Volc. Soc. Japan 20, 229–240.
Newman, S., Lowenstern, J.B., 2002. VolatileCalc: a silicate melt-H_2O-CO_2 solution model written in Visual basic for Excel. Comput. Geosci. 28, 597–604.
Newman, S., Epstein, S., Stolper, E.M., 1988. Water, carbon dioxide, and hydrogen isotopes in glasses from the ca. 1340 a.D. eruption of the Mono Craters, California: constraints on degassing phenomena and initial volatile content. J. Volcanol. Geotherm. Res. 35, 75–96.
Nolan, G.S., Bindeman, I.N., 2013. Experimental investigation of rates and mechanisms of isotope exchange (O, H) between volcanic ash and isotopically-labeled water. Geochim. Cosmochim. Acta 111, 5–27.
Oliva-Urcia, B., Gil-Pena, I., Maestro, A., López-Martinez, J., Galindo-Zaldivar, J., Soto, R., Gil-Imaz, A., Rey, J., Pueyo, O., 2015. Paleomagnetism from Deception Island (south Shetlands archipelago, Antarctica), new insights into the interpretation of the volcanic evolution using a geomagnetic model. Int. J. Earth Sci. 1–18.
Orheim, O., 1972. A 200-Year Record of Glacier Mass Balance at Deception Island, Southwest Atlantic Ocean, and its Bearing on Models of Global Climate Change. vol. 118 Institute of Polar Studies, Ohio State University.
Padrón, E., Pérez, N.M., Hernández, P.A., Sumino, H., Melián, G.V., Barrancos, J., Nolasco, D., Padilla, G., Dionis, S., Rodríguez, F., Hernández, I., Calvo, D., Peraza, M.D., Nagao, K., 2013. Diffusive helium emissions as a precursory sign of volcanic unrest. Geology 41, 539–542.
Parruzot, B., Jollivet, P., Rébiscoul, D., Gin, S., 2015. Long-term alteration of basaltic glass: mechanisms and rates. Geochim. Cosmochim. Acta 154, 28–48.
Pedrazzi, D., Aguirre-Díaz, G., Bartolini, S., Martí, J., Geyer, A., 2014. The 1970 eruption on Deception Island (Antarctica): eruptive dynamics and implications for volcanic hazards. J. Geol. Soc. 171, 765–778.
Pedrazzi, D., Németh, K., Geyer, A., Álvarez-Valero, A.M., Aguirre-Díaz, G., Bartolini, S., 2018. Historic hydrovolcanism at Deception Island (Antarctica): implications for

eruption hazards. Bull. Volcanol. 80, 11.
Roobol, M.J., 1980. A model for the eruptive mechanism of Deception Island from 1820 to 1970. BAS Bull. 49, 137–156.
Roobol, M.J., 1982. The volcanic hazard at Deception Island, South Shetland Islands. BAS Bull. 51, 237–245.
Rosado, B., Fernández-Ros, A., Berrocoso, M., Prates, G., Gárate, J., de Gil, A., Geyer, A., 2019. Volcano-tectonic dynamics of Deception Island (Antarctica): 27 years of GPS observations (1991–2018). J. Volcanol. Geotherm. Res. 381, 57–82.
Sano, Y., Kagoshima, T., Takahata, N., Nishio, Y., Roulleau, E., Pinti, D.L., Fischer, T.P., 2015. Ten-year helium anomaly prior to the 2014 Mt Ontake eruption. Sci. Rep. 5, 13069.
Schipper, C.I., Castro, J.M., Tuffen, H., James, M.R., How, P., 2013. Shallow vent architecture during hybrid explosive-effusive activity at Cordón Caulle (Chile, 2011–12): evidence from direct observations and pyroclast textures. J. Volcanol. Geotherm. Res. 262, 25–37.
Seligman, A.N., Bindeman, I.N., Watkins, J.M., Ross, A.M., 2016. Water in volcanic glass: from volcanic degassing to secondary hydration. Geochim. Cosmochim. Acta 191, 216–238.
Sharp, Z.D., 1990. A laser-based microanalytical method for the in situ determination of oxygen isotope ratios of silicates and oxides. Geochim. Cosmochim. Acta 54, 1353–1357.
Shaw, A.M., Hauri, E.H., Fischer, T.P., Hilton, D.R., Kelley, K.A., 2008. Hydrogen isotopes in Mariana arc melt inclusions: implications for subduction dehydration and the deep-Earth water cycle. Earth Planet. Sci. Lett. 275, 138–145.
Sheppard, S.M.F., 1977. The identification of the origin of ore-forming solutions by the use of stable isotopes. In: Volcanic Processes in Ore Genesis. Inst. Mining and Metallurgy and Geol. Soc, London, pp. 25–41.
Smellie, J.L., 2001. Lithostratigraphy and volcanic evolution of deception island, South Shetland Islands. Antarct. Sci. 13, 188–209.
Smellie, J.L., 2002a. Geology. In: López-Martínez, J., Smellie, J.L., Thomson, J.W., Thomson, M.R.A. (Eds.), Geology and Geomorphology of Deception Island. BAS GEOMAP Series, Sheets 6-a and 6-B, 1:25 000 British Antarctic Survey, Cambridge, pp. 11–30.
Smellie, J.L., 2002b. Volcanic hazard. In: López-Martínez, J., Smellie, J.L., Thomson, J.W., Thomson, M.R.A. (Eds.), Geology and Geomorphology of Deception Island. British Antarctic Survey, Cambridge, pp. 47–53.
Smith, R.K., Tremallo, R.L., Lofgren, G.E., 2001. Growth of megaspherulites in a rhyolitic vitrophyre. Am. Mineral. 86, 589–600.
Stroncik, N.A., Schmincke, H., 2002. Palagonite – a review. Int. J. Earth Sci. 91, 680–697.
Taylor Jr., H.P., Sheppard, S.M.F., 1986. Igneous rocks: I. Processes of isotopic fractionation and isotopic systematics. In: Valley, J.W., Taylor Jr.H.P., O'Neil, J.R. (Eds.), Stable Isotopes in High-Temperature Geological Processes. Reviews in Mineralogy, vol. 16. Mineralogical Society of America, pp. 227–271.
Taylor, B.E., Eichelberger, J.C., Westrich, H.R., 1983. Hydrogen isotopic evidence of rhyolitic magma degassing during shallow intrusion and eruption. Nature 306, 541–545.
The Polar Rock Repository (PRR), Byrd Polar and Climate Research Center (BPCRC), Ohio State University: Polar Rock and Dredge Samples Available for Research and Educational Use from the PRR. doi:https://doi.org/10.7289/V5RF5S180 (date of access).
Torrecillas, C., Berrocoso, M., García-García, A., 2006. The multidisciplinary scientific information support system (SIMAC) for Deception Island, 397–402. In: Fütterer, D.K., Damaske, D., Kleinschmidt, G., Miller, H., Tessensohn, F., eds (Eds.), Contributions to global earth sciences (Springer), Antarctica, pp. 397–402.
Torrecillas, C., Berrocoso, M., Felpeto, A., Torrecillas, M.D., Garcia, A., 2013. Reconstructing palaeo-volcanic geometries using a Geodynamic Regression Model (GRM): application to Deception Island volcano (South Shetland Islands, Antarctica). Geomorphology 182, 79–88.
Tuffen, H., Owen, J., Denton, J.S., 2010. Magma degassing during subglacial eruptions and its use to reconstruct palaeo-ice thicknesses. Earth Sci. Rev. 99, 1–18.
Valencio, D.A., Mendía, J.E., Vilas, J.F., 1979. Paleomagnetism and K-Ar age of Mesozoic and Cenozoic igneous rocks from Antarctica. Earth Planet. Sci. Lett. 45, 61–68.
Valle, N., Verney-Carron, A., Sterpenich, J., Libourel, G., Deloule, E., Jollivet, P., 2010. Elemental and isotopic (^{29}Si and ^{18}O) tracing of glass alteration mechanisms. Geochim. Cosmochim. Acta 74, 3412–3431.
Vergiolle, S., Jaupart, C., 1986. Separated two-phase flow and basaltic eruptions. J. Geophys. Res. 91, 12842–12860.